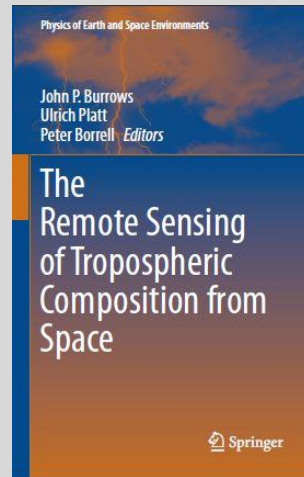**The Remote Sensing of Tropospheric Composition from Space**

Editors:
John P. Burrows
Ulrich Platt
Peter Borrell

Pages 67 to 122

Chapter 2

Solar Backscattered Radiation: UV, Visible and Near IR – Trace Gases

Andreas Richter and Thomas Wagner

Chapter 2
The Use of UV, Visible and Near IR Solar Back Scattered Radiation to Determine Trace Gases

Andreas Richter and Thomas Wagner

2.1 Basics and Historical Background

Satellite remote sensing in the near-IR, visible and UV spectral range makes use of absorption and emission processes of electromagnetic radiation corresponding to electronic transitions, combined with simultaneous rotational-vibrational molecular transitions. One important difference compared to atmospheric observations in the microwave and thermal IR spectral range is that, usually thermal emission can be neglected at short wavelengths (there might, however, be emissions from, for example, excited gases in the high atmosphere). Thus the observed spectral signatures can be directly related to *absorption* spectra of atmospheric constituents. The neglect of emission terms makes the spectral analysis in the UV/vis spectral range usually reasonably straight forward. Another important and related advantage is that from satellite observations in the UV/vis spectral region, information from all atmospheric height layers (including the near surface layers) can be obtained. This makes UV/vis satellite observations a powerful tool for the monitoring of atmospheric pollution and for the characterisation and quantification of emission sources which are usually located close to the ground. It should, however, also be noted that, in contrast to observations in the microwave or thermal IR, usually little or no information on the vertical distribution of a trace gas is obtained.

The analysis procedures applied to satellite observations in the UV/vis/NIR spectral range have evolved from those of ground-based, ship, aircraft or balloon-borne observations, which have been successfully performed over several decades before instruments were placed on orbiting satellites in space. A brief overview of the major developments in this field during the last century is given below.

A. Richter (✉)
Institute of Environmental Physics, University of Bremen, Bremen, Germany

T. Wagner (✉)
Max-Planck-Institute for Chemistry, Mainz, Germany

In 1879, Marie Alfred Cornu proposed that the short wavelength limit of the solar radiation on the Earth's surface must be caused by an absorber located in the Earth's atmosphere. Just a year later, Sir Walther Noel Hartley described the strong UV absorptions between 200 and 300 nm and it became obvious that the absorbing properties of ozone, O_3, fulfilled the requirements of the postulated atmospheric absorber. Additional electronic bands of the O_3 absorption spectrum were discovered in the following years by J. Chappuis and Sir William Huggins (see Fig. 2.1). In 1902 Leon Teisserenc de Bort and Richard Aßmann discovered that the atmospheric temperature starts to increase above about 10 km and in 1908 Teisserenc de Bort called this layer between about 10 km and 50 km the stratosphere. This temperature increase was consistent with the assumption that an absorbing (i.e. O_3) layer exists at these altitudes. In 1925 G. Dobson developed a new very stable spectrophotometer (a double monochromator using quartz prisms and a photomultiplier) for the quantification of the vertically integrated atmospheric concentration or vertical column density, VCD, of O_3. Today the "thickness" of the atmospheric O_3 layer is still expressed in Dobson units (DU), which are defined as the thickness of the atmospheric O_3 vertical column density under standard conditions for temperature and pressure (STP: 293.15K, 1013.25 hPa), measured in 10^{-5} m. Thus, 1 DU of O_3 is equivalent to a column density of 2.68×10^{16} molecules/ cm^2. Dobson spectrometers use a simple (but stable) spectroscopic method: the direct or scattered solar intensity is measured in different narrow (~1 nm) spectral intervals of which some are located inside and some outside the O_3 (Huggins) absorption bands (see Fig. 2.1). From the ratio of the radiation at different wavelengths (and a geometric correction factor accounting for the effect of varying solar zenith angle, SZA) the thickness of the O_3 layer is determined. The impact of absorption and scattering by aerosols or SO_2 on the O_3 retrieval can be accounted
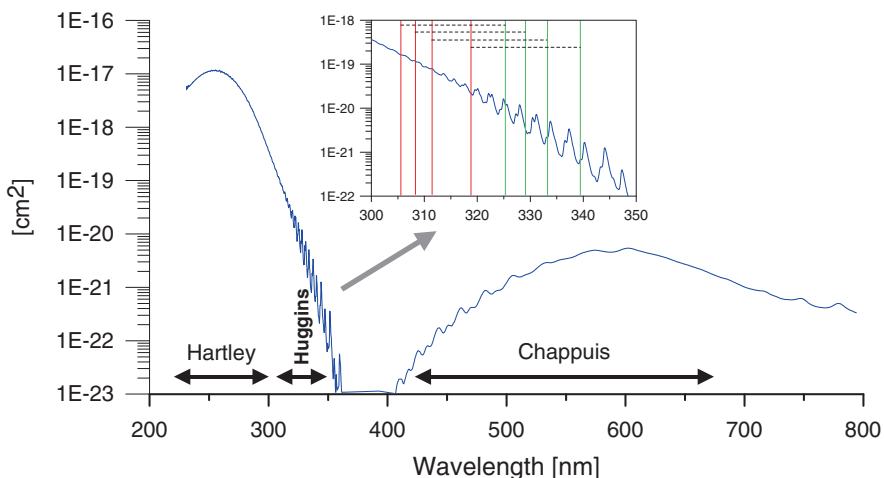

Fig. 2.1 The O_3 absorption cross-section (Bogumil et al. 2003). The highly structured O_3 Huggins Bands are displayed in the panel with an expanded wavelength scale. Also shown in the panel are the wavelength pairs used by Dobson spectrometers (see text).

for by combining different wavelength pairs, for which the influence of O_3 and such interfering effects are different. Dobson spectrometers became widely used and, as a result of an initiative in the international Geophysics Year in 1957 by the International Ozone Commission, a global network of more than 100 instruments was established (Komhyr et al. 1989): the majority still being in use. These instruments provide data over long time, an important basis for the investigation of the long term evolution of the atmospheric O_3 layer.

In 1973 Alan Brewer used a similar method to measure the atmospheric nitrogen dioxide, NO_2, column density from the ground (Brewer et al. 1973). His instrument observes light in different narrow wavelength intervals around 450 nm, for which the NO_2 absorption varies strongly with wavelength. Although the atmospheric NO_2 absorptions are by far weaker than those of O_3, it was possible to identify them with this new spectrometer. It was, in particular, possible to confirm the permanent presence of NO_2 in the stratosphere. One peculiarity of the Brewer spectrometers is that they can also measure O_3 using the light of a full moon when the sky is clear; this is useful in the polar winter. Similar to the Dobson instruments, a network of Brewer spectrometers was established which is still in operation.

Two significant advances with respect to the retrieval of "weak atmospheric absorbers", were introduced in 1975 by Noxon (1975). First, he measured the sky radiances over a continuous spectral interval covering the targeted atmospheric absorption, in this case around 440 nm for NO_2. Secondly he removed the strong structures of the solar Fraunhofer lines (Kirchhoff 1859) (see Fig. 2.3) by dividing a spectrum taken either during sunset or sunrise by another spectrum measured at noon for which the atmospheric light path is much shorter. The difference in the NO_2 absorption of both spectra is a good approximation for the stratospheric NO_2 amount.

In 1976 U. Platt and D. Perner introduced the DOAS (Differential Optical Absorption Spectroscopy) method (Perner et al. 1976; Platt et al. 1979; Perner and Platt 1979), which was first applied to tropospheric observations using artificial light sources. The key concept of DOAS is the simultaneous fit of several trace gas absorption spectra to the measured atmospheric spectrum using only the high frequency part (Platt 1994). This concept is an elegant way to deal with possible spectral interference between absorption structures of different trace gases (e.g. between sulfur dioxide, SO_2, and O_3 for Dobson measurements) and the effects of atmospheric scattering.

After the discovery of the stratospheric O_3 hole in 1985 (Farman et al. 1985), DOAS observations of scattered solar radiation in zenith viewing direction became very important for the monitoring of stratospheric NO_2 and the halogen oxides, BrO and OClO (Solomon et al. 1987). The weak absorption features of these species (typically $< 0.1\%$) could be identified during twilight, when the light paths through the stratosphere are especially long. Today, DOAS observations of scattered sun light are often also performed at a variety of additional viewing directions. The so called Multi AXis (MAX) DOAS observations collect the light at slant elevation angles making such observations especially sensitive to tropospheric trace gases and aerosols.

2.1.1   Satellite Observations in the UV/vis/NIR Spectral Range

Shortly after the launch of the first satellite (Sputnik in 1957), the new space borne platforms were used for observing our planet. In 1960, the first UV/vis image of the Earth's surface and atmosphere was taken by TIROS-1; a few years later, composite images of the whole Earth and the Earth seen as a blue planet from the moon enabled a completely new view of the Earth in space. Satellite images are now widely used, today's instruments typically providing measurements at various spectral intervals, thus allowing the retrieval of a variety of atmospheric and surface properties.

After early conceptual studies and prototype measurements, long-term spectro-scopic UV/vis observations from space started in 1970 on board the US research satellite Nimbus 4 (Heath et al. 1973). These instruments [Backscatter Ultraviolet, BUV, later also called Solar BUV or SBUV, see (Frederick et al. 1986)] operated in nadir geometry i.e. pointing downward to the surface and measuring the solar light reflected from the ground or scattered from the atmosphere (Fig. 2.2). The atmospheric penetration depth of the observed light depends on the optical thick-ness of the atmosphere. Typically most of the observed photons have traversed the stratosphere twice and thus the sensitivity to stratospheric absorbers is high. In the UV, the sensitivity for trace gases close to the surface is usually much lower (except over ice and snow) and for trace gases located below thick clouds it can become almost zero.

In a similar way to the Dobson instruments, the BUV/SBUV also measured the intensity in narrow spectral intervals, for which the atmospheric O_3 absorption differs. From the BUV/SBUV data it is possible to retrieve information on the atmospheric O_3 concentration profile, because the penetration depth into the atmo-sphere strongly depends on the absolute value of the O_3 absorption cross-section and thus on wavelength (see Fig. 2.1). Typically, the received light at the shortest wavelengths has only "seen" the highest parts of the O_3 layer whereas the longest wavelengths have seen the total column.

Like the BUV/SBUV instruments, the TOMS instruments [Total Ozone Mapping Spectrometer, first launched in 1979 on Nimbus 7, (Heath et al. 1975)] observe the backscattered light in distinct wavelength intervals, but at longer wavelengths, for which the light can penetrate the whole atmosphere. TOMS observations thus yield the total O_3 VCD, constituting a major breakthrough in UV/vis satellite remote sensing. The TOMS instrument on board Nimbus 7 has yielded the longest continuous global data set on the O_3 layer (1979–1992) (McPeters et al. 1996), covering in particular the formation and evolution of the ozone hole. Since then, several further TOMS instruments were launched on other satellites.

A completely new quality of the observed spectral information became available in 1995 with the launch of the first DOAS-type instrument, the Global Ozone Monitoring Experiment (GOME) on the European research satellite ERS-2 (ESA 1995; Burrows et al. 1999 and references therein). Similar to SBUV and TOMS, GOME is a nadir viewing instrument, but it contiguously measures a large spectral
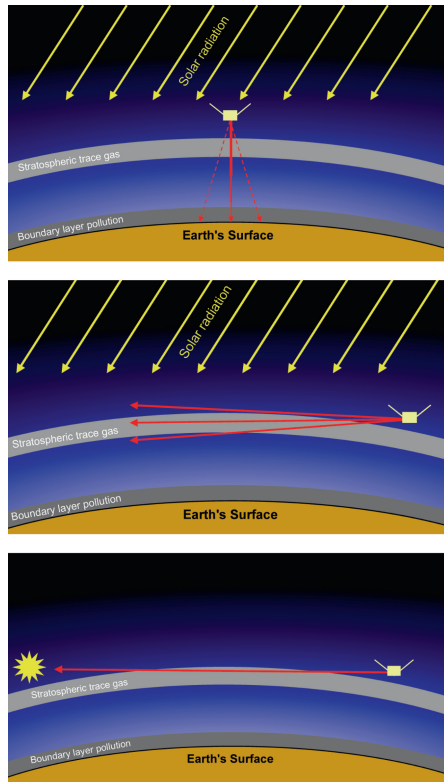
Fig. 2.2 Different viewing geometries for satellite observations in the UV/vis/NIR spectral range (thickness of the atmosphere and altitude of the satellite are not to scale). *Top*: in nadir mode (often the actual viewing angles also include more slant angles) the satellite instrument measures sun light which is reflected from the surface or scattered in the atmosphere. Such measurements are sensitive not only for stratospheric trace gases, but also for trace gases close to the surface. *Middle*: in limb mode scattered sunlight is observed at several almost horizontal viewing angles. Such observations are very sensitive to stratospheric trace gas profiles. *Bottom*: in occultation geometry, the direct light of sun, moon, or stars is observed. Occultation observations can also be performed during night. In contrast to limb and nadir observations, the light path is well defined.

range (237–793 nm, see Fig. 2.3, having a spectral resolution between 0.2 and 0.4 nm. The spectral range is sampled at a total of 4,096 wavelengths arranged in four "channels". Its standard ground pixel size is 320×40 km² (East-West $\times$ North-South) enabling global coverage to be achieved each 3 days.

In contrast to the few spectral intervals measured by BUV/SBUV and TOMS instruments, GOME spectra yield a plethora of spectral information. In the reflectance spectra not only are the broad band signatures of atmospheric scattering and surface reflectivity observed, but also the detailed features of some strong atmospheric absorbers (e.g. O_3, H_2O, and O_2) can be seen directly (Fig. 2.3). By applying the DOAS method, it has been possible to analyse the atmospheric absorptions of a
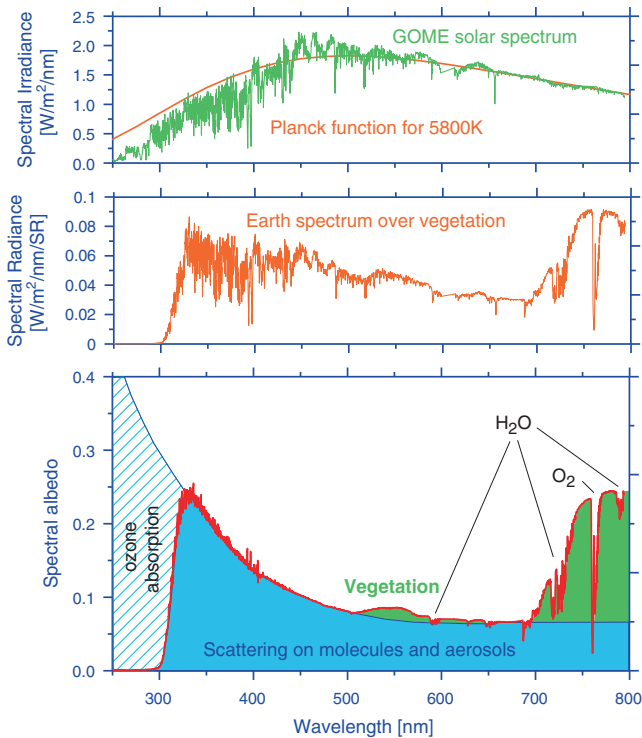
Fig. 2.3 *Top*: solar spectrum (*green*) measured by GOME containing a variety of solar Fraunhofer lines. For comparison, the black-body radiation for 5,800 K is also shown (note that the sun is not a perfect black body; also the radiation in certain parts of the spectrum originates from layers at different temperatures). *Middle*: "earth shine" spectrum of solar radiation reflected and scattered by the Earth's surface and atmosphere (clear sky over vegetation). *Bottom*: the spectral reflectance (*red curve*) calculated from both spectra. The broad band spectral dependence reflects the effects of scattering on air molecules (and aerosols). Atmospheric trace gas absorptions of O_3, O_2, and H_2O are also evident. Enhanced values in the *green* and in the near IR spectral range are due to increased reflectance over vegetation.

large variety of weak atmospheric absorbers such as NO_2, BrO, chlorine dioxide, OClO, formaldehyde, HCHO, glyoxal, CHOCHO, iodine monoxide, IO, the oxygen dimer, O_4, and SO_2, many of them located close to the Earth's surface. In addition, other quantities like aerosol extinction, cloud properties, surface albedo, vegetation properties, ocean colour, and indices characterising the solar cycle are retrieved from the GOME measurements.

In March 2002 the SCanning Imaging Absorption SpectroMeter for Atmospheric CHartographY (SCIAMACHY) (Burrows et al. 1988; Burrows et al. 1995; Bovensmann et al. 1999) was launched on board the European research satellite ENVISAT. Compared to GOME, its spectra cover a wider wavelength range (214–2380 nm), facilitating measurements of the absorption of several greenhouse gases (CO_2, CH_4, and nitrous oxide, N_2O) and the pollutant carbon monoxide,

CO, in the Near-IR spectral region. In addition to nadir viewing, SCIAMACHY also makes observations in limb and solar and lunar occultation geometry, which yield profiles of stratospheric and mesospheric trace constituents (see Fig. 2.2). Another advantage is that the ground pixel size for the nadir viewing mode is appreciably reduced to 30×60 km² (and in a special mode to 15×30 km²). For the observation of tropospheric trace gases this is most important, because their concentrations can exhibit strong spatial gradients. Smaller ground pixels are also less affected by clouds (Krijger et al. 2007).

In 2004, the Ozone Monitoring Instrument (OMI) was launched (Levelt and Noordhoek 2002). Compared to GOME and SCIAMACHY, it has a limited spectral range (270–500 nm), but a higher spatial resolution (up to 13×24 km²) in nadir viewing mode. Together with its daily global coverage, it provides unprecedented detail of the spatio-temporal variability of tropospheric trace gases. In October 2006, the first of three instruments of a second generation of GOME instruments was launched on MetOp 1. The two other GOME-2 instruments are scheduled for launch at time intervals of 5 years for the MetOp 2 and MetOp 3 platforms, thus extending the time series of GOME, SCIAMACHY, and OMI into the next two decades (EUMETSAT 2005). Compared to GOME-1, the GOME-2 instruments have an almost daily global coverage and much improved spatial resolution (80×40 km²).

2.1.2 Spectral Retrieval and Radiative Transfer Modelling

As mentioned above, one important advantage for the retrieval of data products from atmospheric observations in the UV/vis/NIR spectral range is that emission terms can usually be neglected. The measured spectral signatures can be directly related to the absorption spectra of different atmospheric trace gases within the chosen spectral range. In practice, the data analysis usually comprises two steps. First, the spectra are analysed using, for example, the DOAS method: based on Beer-Lambert's law, the spectral analysis yields the trace gas concentration along the atmospheric light path or more precisely the average over all contributing light paths (see Fig. 2.5). For historical reasons the result is nevertheless called slant column density, SCD. In the second step, by taking into account the viewing geometry and scattering, absorption and reflection within the atmosphere and at the Earth's surface, the trace gas SCD is converted into a more useful quantity, that is the VCD, or the trace gas concentration. Usually, for this conversion, numerical atmospheric radiative transfer simulations have to be performed.

The separation of spectral retrieval and radiative transfer modelling has the advantage that it is conceptually simple, and possible retrieval errors can be easily identified and corrected. Nevertheless, it should be noted that this separation is strictly valid only for cases with well-defined atmospheric light paths, such as satellite observations in occultation viewing geometry (Fig. 2.2). For the observation of scattered and reflected light (e.g. up welling from the top of the atmosphere),

many different atmospheric light paths contribute to the measured spectra. This causes non-linearities between the measured absorptions and the corresponding atmospheric column densities (Van Roozendael et al. 2006). However, except for strong absorbers (such as O_3, H_2O or CO_2), these non-linearities are small and can usually be neglected (see Section 2.2.4). More details on the spectral analysis and atmospheric radiative transfer modelling are provided in the following sections.

2.2 Spectral Retrieval

The retrieval of information on atmospheric trace species from measurements in the UV/vis/NIR utilises Beer–Lambert's law:

$$dI(\lambda) = -I(\lambda)\sigma(\lambda)\rho(s)ds \qquad (2.1)$$

This states that for an infinitesimally thin layer, the change in intensity at a given wavelength λ is proportional to the intensity I, the absorption cross-section σ, the absorber number density ρ and the light path element ds.

After reaching the atmosphere, light from the sun is either scattered by molecules, particles or cloud droplets, or is reflected at the surface towards the observing satellite instrument. Along its path through the atmosphere, part of the light is absorbed by trace species and the resulting reduction in intensity can be used to determine the amount of the species present in the atmosphere. In contrast to other spectral regions, the atmosphere is nearly transparent over large parts of the UV/visible/NIR part of the spectrum. As a result, nadir satellite measurements have sensitivity from the top of the atmosphere down to the surface albeit with varying efficiency. Rayleigh scattering is a strong function of wavelength, and is the dominant extinction process in the UV outside the strong O_3 absorption bands. At short wavelengths (below about 300 nm), O_3 absorption in the stratosphere becomes even stronger, eventually blocking the view from space down to the troposphere. Particle scattering from aerosols is efficient in the UV/vis/NIR spectral range, as is scattering from cloud droplets. For simplicity, this type of scattering is often approximated by Mie theory, although only liquid aerosols or small cloud droplets are strictly spherical. Any retrieval of atmospheric concentrations of a trace species in this spectral region has therefore to account for absorption by molecules, Rayleigh scattering, Mie scattering and surface reflection.

In the UV/vis spectral range, molecular spectra are dominated by electronic transitions and their vibrational structures. In contrast to other wavelength regions, the spectra are quasi-continuous, since most molecules (in particular those containing more than two atoms) have a very large number of overlapping rotational lines, and some are also affected by pre-dissociation. Due to the resulting "band structure" of most molecular spectra, high spectral resolution is usually not required to resolve the cross-sections. This also implies that no vertical information is available from the shape of rotational lines, as is the case for example in the microwave

Table 2.1 Overview of the tropospheric trace species retrieved from measurements of the UV/vis/NIR radiance by nadir viewing satellite instruments, and the spectral windows typically used

Trace species	Typical spectral window used
SO_2	315–327 nm
O_3	325–335 nm
BrO	345–359 nm
HCHO	334–348 nm
IO	416–430 nm
NO_2	425–450 nm
CHOCHO	436–457 nm
H_2O	610–730 nm
CO	2,324–2,335 nm
CH_4	1,629–1,671 nm
CO_2	1,558–1,594 nm

region (see Chapters 1 and 4). The number of species which can be observed in the UV/vis is limited but includes a number of key players in atmospheric chemistry, e.g. O_3, NO_2, HCHO and halogen oxides (see Table 2.1). Towards the IR part of the spectrum, some line absorbers such as O_2, H_2O, CO_2, CH_4, CO have spectral features and can also be retrieved.

In recent years satellite instruments covering the UV/vis/NIR spectral range have evolved from having a few discrete channels with low spectral resolution, to instruments with wide and continuous spectral coverage at moderate spectral resolution. While the latter can usually resolve the relevant structures in the UV and visible range, they cannot resolve the rotational line spectra, in particular in the NIR. This leads to some complications in the data analysis which are discussed later in this section.

Many data analysis approaches used in the UV/visible spectral range separate the retrieval of the amounts of atmospheric constituents into two steps as mentioned before: first, the trace gas concentration $\rho(s)$ of the absorber integrated along the light path s is determined applying Beer-Lambert's law to the spectra. The resulting slant column density, *SCD,*

$$SCD = \int \rho(s)ds \qquad (2.2)$$

is then converted to a vertical column density, *VCD,* integrated from the surface to the top of atmosphere, *TOA*,

$$VCD = \int_0^{TOA} \rho(z)dz \qquad (2.3)$$

by simulating the effective light paths with a radiative transfer model. This is usually achieved by invoking airmass factors (AMFs), which are discussed in detail in Section 2.3.2. The underlying assumption is that the light path is determined by geometry, scattering from air molecules, aerosols and clouds, as well as surface reflection, but is independent of the amount and vertical distribution of the absorber

itself. This is valid for small absorptions (less than a few percent), but for strong absorbers, the retrieval has to be modified as will be discussed in Section 2.2.4.

2.2.1 Discrete Wavelength Techniques

When applying Beer–Lambert's law to atmospheric measurements, three problems need to be addressed:

- What is the initial intensity I_0 at the top of atmosphere?
- How can the effects of different absorbers, scattering and surface reflectance be separated?
- What is the (effective) length of the light path?

a   Initial Intensity I_0

Typically satellite instruments make measurements of I_0 by observing the sun without the atmosphere, using a diffuser to reduce light intensity. Therefore, the initial intensity I_0 can be assumed to be known. In practice, instrument degradation related to the diffusers used can be a problem (Hilsenrath et al. 1995), but this will not be discussed here.

A complication is introduced for measurements using scattered light. In this case, the initial intensity does not only depend on I_0 but also on the scattering efficiency in the atmosphere, and, for nadir measurements, on the surface reflectivity. Neither quantity is usually well known. As will be described later, this problem can be solved by using several wavelengths simultaneously and assuming that the change of scattering efficiency with wavelength is small or well known.

b   Separating Different Effects

The second point for separating effects (different absorbers, scattering and surface reflectance) can be achieved by using measurements at several wavelengths. To illustrate this, a simplified view of radiative transfer through the atmosphere is considered.

Assuming that the only effect of significance is the absorption by one gas, the intensity measured at the satellite follows from the integrated form of the Beer–Lambert's law (Eq. 2.1):

$$I(\lambda) = cI_0(\lambda) \exp\left\{ - \int \sigma(\lambda)\rho(s)ds \right\} \qquad (2.4)$$

where c is an efficiency factor accounting for the fact that scattered light is being measured. This factor c depends not only on the surface reflectance but also on the scattering in the atmosphere and the presence of clouds. If in addition, extinction by Rayleigh and Mie scattering is considered and the absorption cross-section is assumed not to vary along the light path, we obtain:

$$I(\lambda) = cI_0(\lambda) \exp\left\{ -\sigma(\lambda) \int \rho(s)ds - \sigma_{Ray}(\lambda) \int \rho_{Ray}(s)ds - \sigma_{Mie}(\lambda) \int \rho_{Mie}(s)ds \right\}$$

(2.5)

where σ_{Ray} is the Rayleigh extinction cross-section, σ_{Mie} is the Mie extinction cross-section and ρ_{Ray} and ρ_{Mie} are the number densities of Rayleigh and Mie scatterers, respectively.

Substituting the definition of the slant column density SCD (Eq. 2.2), the expression for the received intensity (Eq. 2.5) reads:

$$I(\lambda) = cI_0(\lambda) \exp\left\{ -\sigma(\lambda)SCD - \sigma_{Ray}(\lambda)SCD_{Ray} - \sigma_{Mie}(\lambda)SCD_{Mie} \right\}.$$ (2.6)

We now assume that measurements are made at two selected wavelengths: one, where the absorber of interest has a strong absorption, and the other where the absorber has no absorption or only weak absorption. If one can model the wavelength dependence of scattering with reasonable accuracy, then these two measurements can be used to determine the SCD for the absorber of interest. This is basically the approach used for the retrieval of the total column density of O_3 from the measurements by the TOMS instrument.

When several absorbers are present, we have to extend formula in Eq. 2.6 to:

$$I(\lambda) = cI_0(\lambda) \exp\left\{ -\sum_i \sigma_i(\lambda)SCD_i - \sigma_{Ray}(\lambda)SCD_{Ray} - \sigma_{Mie}(\lambda)SCD_{Mie} \right\}$$ (2.7)

where i is the index of the different absorbers. Measurements at more wavelengths are needed to separate the signals. With this technique, not only O_3 but also SO_2 column densities can be retrieved from measurements of the TOMS instrument, provided the loading of SO_2 is large enough, for example in volcanic plumes.

c   The Light Path

The third aspect, the length of the light path, or more precisely the average length of the ensemble of all possible light paths, is determined by using radiative transfer calculations which are discussed in Section 2.3.

The use of discrete wavelengths for measurements of atmospheric O_3 column densities has been applied successfully since the launch of the BUV satellite and extensively using the data from the TOMS instruments (Heath et al. 1978). This technique has the advantage of a relatively simple instrument with good signal to noise ratio, and builds on the heritage of the ground-based Dobson spectrophotometer and its network. As the number of discrete wavelengths used is small, the retrieval algorithms are fast and relatively simple, in particular if pre-calculated values are used for the weighting factors accounting for different atmospheric scenarios and the treatment of surface effects and clouds. By refining these lookup tables based on extensive validation, excellent agreement with ground-based measurements was achieved for the total column densities of O_3. The approaches used to derive the tropospheric O_3 column density from the TOMS measurements is described in Section 2.4. The disadvantage of these measurements is the small number of spectral measurement points. If another signal interferes, there is simply not enough information to separate the effects. This limits the application to strong absorbers with little interference from other effects. Also, for trace gases other than O_3 and SO_2, the exact wavelength positions of the TOMS spectral channels are not suitable. As a result, the method cannot be applied to other trace gases with smaller absorption such as BrO, NO_2 or HCHO.

2.2.2 DOAS Type Retrievals

In order to extend the measurements to weaker signals and more species, instruments have been developed, which cover a large and quasi-continuous spectral range at moderate resolution, e.g. GOME and SCIAMACHY. Such measurements are usually analysed using the Differential Optical Absorption Method (DOAS) which was initially developed for ground-based measurements (Noxon 1975; Platt et al. 1979; Solomon et al. 1987). The basic idea of DOAS is to separate the wavelength dependent absorption signal into two components, the low frequency part and the high frequency part. The high frequency part of the spectrum is used for the retrieval of atmospheric absorptions, while the low frequency part is treated as a closure term and is approximated by a low order polynomial or other smooth function.

In practice, the absorption cross-sections of the absorbers are separated into the slowly varying part $\sigma^*(\lambda)$ and the differential part $\sigma'(\lambda)$: $\sigma(\lambda) = \sigma^*(\lambda) + \sigma'(\lambda)$:

$$I(\lambda) = cI_0(\lambda) \exp \left\{ -\sum_i \sigma_i'(\lambda) SCD_i - \sum_i \sigma_i^*(\lambda) SCD_i \right.$$
$$\left. -\sigma_{Ray}(\lambda) SCD_{Ray} - \sigma_{Mie}(\lambda) SCD_{Mie} \right\}. \qquad (2.8)$$

Both the Rayleigh and Mie scattering cross-sections can be approximated by a polynomial in wavelength so that the three slowly varying contributions to the signal are combined into one closure polynomial, which in addition can compensate, in part, for any wavelength dependent changes in the throughput of the instrument:

$$I(\lambda) = cI_0(\lambda) \exp\left\{ -\sum_i \sigma_i'(\lambda)SCD_i - \sum_p a_p\lambda^p \right\} \qquad (2.9)$$

This equation is often written as a function of optical depth $\ln (I_0/I)$

$$\ln \frac{I_0(\lambda)}{I(\lambda)} = \sum_i \sigma_i'(\lambda)SCD_i + \sum_p c_p\lambda^p. \qquad (2.10)$$

This links the measurement signal (the optical depth) in a linear equation with the quantities of interest (the slant column densities SCD_i) and a closure polynomial, which also accounts for the factor c, assuming that the logarithm of the scattering efficiency can be approximated by a polynomial. One such equation can be written for each measurement wavelength, and by solving the resulting system of linear equations in a least squares procedure, the best set of slant column densities and polynomial coefficients result. In addition to its simplicity, the DOAS retrieval has the benefit of cancelling all multiplicative effects in I and I_0, which are measured by the same instrument in a short period of time using near identical experimental configuration. This relaxes the requirements for the absolute radiometric calibration of the measured intensities. Other remaining instrumental issues (e.g. the etalon resulting from multi-beam interference in optical components or ice layers on the detectors) and effects such as spectral changes in surface reflectance are at least partly compensated for by the closure polynomial, making this technique very valuable for the detection of small signals.

In some applications, a second closure polynomial is added to the measured intensities to account for instrumental stray light and the effect of inelastic scattering. This correction is non-linear in the optical densities. If only a constant offset c is used, it can be approximated by including another spectrum c/I in the spectral fitting process (Noxon et al. 1979).

One complication arises from the fact that the measured values of the intensity I and I_0 are usually not fully resolved spectrally but are taken at instrument resolution. Therefore, the quantity measured is the intensity convoluted with the instrument slit function. If this is accounted for in Eq. 2.9, the logarithm can no longer simply be taken on both sides of the equation as it cannot be exchanged with the convolution. For most practical applications it is sufficient to apply the convolution with the instrument function to the cross-sections and then to proceed to (Eq. 2.10). However, for strong and structured absorption, a correction has to be applied which is called I_0-correction (Aliwell et al. 2002). For line absorbers the problem is more complex and will be discussed in Section 2.2.4.

DOAS retrievals using data from GOME, SCIAMACHY, OMI, and GOME-2 have been used to determine tropospheric column densities of many trace species, including SO_2, BrO, IO, HCHO, glyoxal, NO_2, and H_2O. The advantage of using continuous spectra is the higher sensitivity that can be achieved, the ability to separate different absorbers, the intrinsic wavelength calibration on the well known Fraunhofer lines in the solar spectrum and the flexibility in the choice of wavelength regions. The disadvantages are the more complex instrumentation, higher data rates resulting in slower retrievals, the need for input data at high spectral resolution and some complicating effects which become more relevant at higher spectral resolution as discussed below. An overview over more effects relevant for the accuracy of scattered light DOAS measurements can be found in Platt et al. (1997) and Platt and Stutz (2008).

2.2.3 Some Considerations for DOAS Retrievals

a Fraunhofer Spectrum

An ideal light source for an atmospheric DOAS measurement would be bright, constant, continuous and without spectral features. While the sun provides sufficient intensity at visible wavelengths and at least over a day can be considered to be a constant light source, it does have many spectral features. These so called Fraunhofer lines are created by absorption by molecules and ions in the solar atmosphere and result in three important demands on the retrievals from space-borne observations: the need for accurate wavelength alignment or spectral calibration, the need for spectral oversampling and the need to correct for the so called Ring effect which is discussed in the next section. In addition the requirements on instrument stability (e.g. with respect to the spectral resolution) are especially high.

As shown previously in Fig. 2.3, the depth of the Fraunhofer lines is of the order of 10–50%, much larger than most absorptions in the Earth's atmosphere, which are often on the per mill level. As a result, even a very small wavelength shift between I and I_0 will result in large structures when the ratio is taken in the DOAS equation, rendering the retrievals of small absorptions impossible. To reduce this effect, two approaches are taken. Firstly, instruments are temperature stabilised as far as possible to reduce spectral shifts induced by temperature changes of the spectrometer. Secondly, the spectra I and I_0 are numerically aligned and interpolated, prior to the fit or, iteratively as part of the retrieval, to minimize any spectral misalignment.

Although satellite instruments are usually well stabilised, the need for spectral alignment arises in some instruments from a difference in observation mode between solar irradiance measurement and nadir observations. For GOME and SCIAMACHY solar observations, the measurements are taken in the flight direction. This results in a small Doppler shift of the spectrum, which has to be compensated for. While the exact magnitude of the effect can be calculated, a full correction is only possible if the sampling of the measurements is several times as good as the spectral resolution

of the instrument (Chance et al. 2005; Roscoe et al. 1996). If that is not the case (as for example in the GOME instrument), the spectra are "under-sampled", and artificial structures are introduced in the interpolated spectra.

b   The Ring Effect

The combination of the highly structured solar spectrum and inelastic scattering processes can lead to an additional effect which is named the Ring effect after one of its discoverers (Grainger and Ring 1962). Elastic scattering (Rayleigh scattering, Mie scattering) does not change the high frequency spectral shape (i.e. intensity variations over wavelength regions of a few nanometres), which is used by the DOAS approach. Therefore, the Fraunhofer lines in I and I_0 are expected to have the same depth and to cancel when the ratio is taken in the DOAS equation. However, observations have shown that the depth of Fraunhofer lines in scattered light is smaller than that in direct solar light, resulting in a highly structured signal in the ratio (Grainger and Ring 1962). The explanation for this effect is inelastic rotational Raman scattering, which distributes the intensity of the scattered photons over several nanometres (Joiner et al. 1995; Kattawar et al. 1981). As the loss of intensity through Raman scattering is proportional to the local intensity, while the gain in intensity is proportional to the intensity at neighbouring wavelengths, the effect is a filling-in of deep Fraunhofer lines in the scattered light spectrum as illustrated in Fig. 2.4. The amount of filling-in depends on the relative amounts of inelastic and elastic scattering and can be simulated with radiative transfer models (RTMs). In the retrieval, it is accounted for by inclusion of a pseudo-absorber (usually referred to as Ring spectrum) computed by an RTM. It should be noted that the spectral
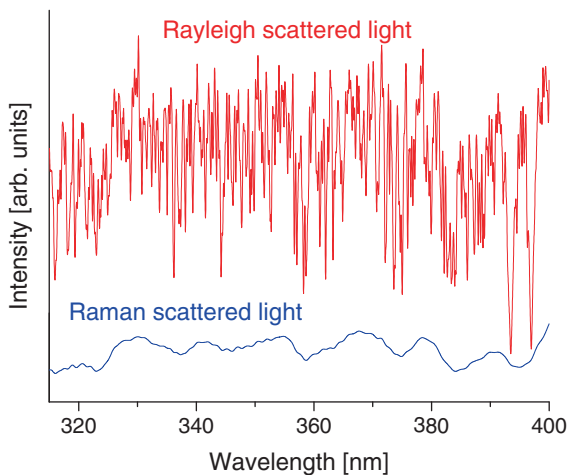

Fig. 2.4 Illustration of the Ring effect. The *upper panel* shows a modelled spectrum of elastically scattered sun light (single Rayleigh scattering) at a spectral resolution of about 0.2 nm. The lower panel shows the modelled spectrum of Raman scattered light. Note that the vertical scales differ: the intensity of the Raman scattered light is only about 4% of that for the elastically scattered light.

shape of inelastically scattered light is relatively smooth and the high frequency component is only introduced by taking the ratio of I and I_0. The strong dependence of the Ring effect on the light path can actually be used to derive information on cloud cover and cloud top height (Park et al. 1986; Joiner and Bhartia 1995; Joiner et al. 1995; deBeek et al. 2001; Joiner and Vasilkov 2006).

A more subtle effect of inelastic scattering is the filling-in of absorption lines of structured absorbers (if the absorption has occurred before the Raman scattering event) (Fish and Jones 1995; Vountas et al. 1998). The effect is similar to that for Fraunhofer lines and can be interpreted as a loss of absorption signal if a photon is scattered inelastically. Therefore, absorption signatures in atmospheric measurements are slightly smaller than expected for an atmosphere without inelastic scattering.

In contrast to rotational Raman scattering, vibrational Raman scattering is a small and negligible effect in the atmosphere. However, in water it can be significant if the light path is long enough. As the energy changes are much larger for vibrational than for rotational transitions, the spectral signature of the two effects is slightly different (Vountas et al. 2003).

c   Choice of Fitting Window

When selecting an appropriate spectral region for the retrieval of a specific trace gas, several considerations have to be taken into account. At first glance, one would assume that the optimum retrieval would use all available information and thus all the spectral points. However, in practice, smaller fitting windows are used for several reasons. The most fundamental argument is that the separation of spectral retrieval and radiative transfer calculation is not valid over large spectral ranges. As result of increasing Rayleigh scattering, light paths change towards the UV and therefore the slant column densities at, for example, 350 nm are not identical to those at 450 nm. This effect leads to a mismatch of measured absorption and fitted absorption cross-sections, resulting in poor fits if not accounted for, as discussed in Section 2.2.4 for strong absorbers. Experience also shows that small inaccuracies in cross-sections of interfering species can lead to large errors for weak absorbers, and by using smaller wavelength regions, such errors can partly be compensated for by the scaling factors and the closure polynomial. Moreover, extending the spectral range always increases the noise, if only relatively weak spectral structures of the desired species are added. Therefore the signal to noise ratio might actually deteriorate upon extending the spectral range. Further considerations sometimes suggest the exclusion of spectral regions where spectra of different trace gases or strong Fraunhofer lines overlap.

Appropriate fitting windows are therefore selected by trying to maximise the differential absorption structures of the molecule of interest and, at the same time, minimizing the impact from interfering signals. This can often be done on simulated data, although the results might not be fully representative for real measurements if absorption cross-sections are inaccurate or not all atmospheric

effects are included in the model. Some examples for fitting windows used in the literature are given in the Table 2.1.

d   Effects of Spectral Surface Reflectivity

In recent years, it became evident that, in addition to trace gas absorptions, the Earth's reflectivity for certain surface types exhibits narrow spectral variations. Examples are absorption features over vegetation in the blue and red spectral range, as well as water absorption structures in the blue spectral range. As mentioned in the previous section, spectral features are caused by vibrational Raman scattering in water (mainly in the UV) and biological activity in the oceans (in the blue and red spectral range) (Vasilkov et al. 2002; Vountas et al. 2003; Vountas et al. 2007; Wagner et al. 2007a; Bracher et al. 2008). Although the amplitude of these spectral structures is usually rather small (in the range of a few percent), they can interfere with trace gas absorption features in the same spectral windows and, if not accounted for, result in large errors in the trace gas results (Vountas et al. 2003; Wagner et al. 2007a). Including the relevant surface spectral features as reference spectra minimizes the interferences. In this way, DOAS analyses of satellite observations can also yield important information on surface properties such as, for example, the primary productivity in sea water (Vountas et al. 2007; Bracher et al. 2008).

2.2.4   Advanced DOAS Concepts

While the DOAS retrieval concept described above is fast and has successfully been used for the analysis of many trace gases, there are situations where the assumptions made are not fulfilled. Modifications to the approach are then needed to achieve accurate results. This is particularly the case in situations where absorption becomes large or the spectral resolution of the instrument is not high enough to resolve the spectrum of line absorbers.

   If absorption by a molecule becomes larger than a few percent, as is the case for atmospheric absorption by O_3 in the Huggins bands, or by SO_2 during volcanic eruptions, the average light path is no longer independent of the absorber amount and its vertical distribution. As a result, the separation of spectral retrieval and light path determination, used in standard DOAS retrieval is no longer applicable. One way of visualising the effect is to compare average light paths at two selected wavelengths, one having strong O_3 absorption and one having weak absorption. Photons experiencing weaker absorption will, on average, penetrate deeper into the atmosphere before they are scattered back to the satellite and therefore have a longer light path than photons at O_3 absorption peaks. This leads to a distortion of the absorption structure observed in the measured optical depth as compared to the simple absorption cross-section, which needs to be taken into account. On the

other hand, this distortion also provides information on the vertical distribution of the observer and is used for example in the BUV retrievals of O_3 and SO_2 profiles (Bhartia et al. 1996; Hoogen et al. 1999; Liu et al. 2005; Yang et al. 2009).

For line absorbers, especially in the NIR, the spectral resolution of the instruments used is often not sufficient to resolve fully the line structure. The measured signal $I_{meas}(\lambda)$ then depends strongly on the instrument transfer function or slit function $F(\lambda)$ of the instrument:

$$I_{meas}(\lambda) = F(\lambda)^* I(\lambda) \tag{2.11}$$

Here, * denotes the convolution of the true intensity with the instrument slit function.

This has implications for the dependence of the measured optical depth on the absorber amount. While for each monochromatic wavelength the Beer–Lambert law applies, the convoluted intensity will no longer be a simple exponential function of the atmospheric trace gas amount in the presence of non-resolved line absorbers. This is the result of the non-interchangeability of exponential function and convolution. As an additional complication, the spectral shape of the measured optical depth changes with light path, absorber amount and temperature.

One solution to these problems is to replace the slant column density SCD by the slant optical depth SOD (Noël et al. 2004; Richter et al. 1999). Starting from Eq. 2.5:

$$I(\lambda) = cI_0(\lambda) \exp\left\{ -\int \sigma(\lambda)\rho(s)ds - \sigma_{Ray}(\lambda)\int \rho_{Ray}(s)ds - \sigma_{Mie}(\lambda)\int \rho_{Mie}(s)ds \right\}$$

one can replace the first term by the slant optical depth:

$$SOD(\lambda) = \int \sigma(\lambda)\rho(s)ds \tag{2.12}$$

and following the same derivation as for the standard DOAS equation, one obtains:

$$\ln\frac{I_0(\lambda)}{I(\lambda)} = \sum_i SOD_i(\lambda) + \sum_p c_p\lambda^p . \tag{2.13}$$

The $SOD_i(\lambda)$ have to be computed using a radiative transfer model for an *a priori* atmosphere and subsequently be convoluted with the instrument's slit function. To a first order approximation, a simple linear scaling of the *a priori* SOD^0 can be used in place of the exact SOD:

$$\ln\frac{I_0(\lambda)}{I(\lambda)} = \sum_i r_i SOD_i^0(\lambda) + \sum_p c_p \lambda^p \tag{2.14}$$

where SOD_i^0 is the slant optical depth for absorber i computed for the *a priori* atmosphere and r_i are the fit parameters and give the ratio of the absorber amount in the measurement relative to the amount in the *a priori* atmosphere.

This approach yields accurate results for O_3, SO_2 and H_2O even at large absorption if the *a priori* assumptions are sufficiently close to the real atmospheric situation. The effect of line absorbers is properly taken into account by the forward calculations at high spectral resolution which are then convoluted to the resolution of the instrument. The requirement is to select appropriate *a priori* assumptions using climatologies or alternatively to iterate those using the column densities retrieved in the first retrieval step and the residuals obtained from the fit.

Another, in some aspects similar but more general, formulation is obtained by introducing weighting functions *WF* (Buchwitz et al. 2000; Rozanov et al. 1998). The weighting function is here defined as the change in the logarithm of the intensity for a change in one of the parameters d_i from their value in the *a priori* assumptions, d_i^0:

$$WF_i(\lambda) = \left.\frac{\partial \ln I(\lambda)}{\partial d_i}\right|_{d_i^0} \tag{2.15}$$

The d_i can be the column density of absorbers but also other parameters such as surface albedo, temperature or aerosols. The logarithm of the intensity can then be developed in a first order Taylor expansion around a modelled intensity I_0^{mod} for the *a priori* atmosphere

$$\ln I(\lambda) = \ln I_0^{\mathrm{mod}}(\lambda) + \sum_i WF_i(\lambda)(d_i - d_i^0) + \sum_p c_p \lambda^p \tag{2.16}$$

The fit parameters are $(d_i - d_i^0)$ and the polynomial coefficients for the broadband structures. As for the SODs, the weighting functions are calculated using radiative transfer models and *a priori* assumptions on the atmosphere, surface albedo etc. They can account for the effects of spectral averaging on line absorbers, for strong absorptions and for other parameters such as surface albedo. Weighting functions have been used for the retrieval of O_3, CO, CO_2, and CH_4. As already mentioned for *SOD*s, the main difficulty lies with the choice of proper *a priori* assumptions as the accuracy of the retrieval is best for small values of $(d_i - d_i^0)$. A further alternative was introduced by Frankenberg et al. (2005) who developed a weighting function algorithm (Iterative Maximum *a priori*, IMAP), which adjusts the *a priori* assumptions iteratively during the analysis.

2.3   Interpretation of the Observations Using Radiative Transfer Modelling

The sensitivity of UV/vis/NIR satellite observations depends on the distribution of the paths of the observed radiation through the atmosphere. Since it is only in nadir viewing geometry that a significant fraction of the observed UV, visible and NIR light penetrates into the lowest atmospheric layers, only nadir observations provide sufficient sensitivity for the observation of tropospheric species. This section therefore concentrates on satellite observations in nadir viewing geometry. In the following, the term nadir viewing geometry is defined to also include viewing directions approximately $\pm 60°$ around nadir. In contrast, observations in limb or occultation viewing geometry provide information from the upper troposphere and above (see Fig. 2.2). The concepts and methods introduced in this section are not restricted to nadir data but can be and are applied to satellite observations in limb and occultation geometry as well.

2.3.1   Relevant Interaction Processes Between Radiation and Matter

A nadir looking satellite instrument in the UV/vis/NIR spectral range measures sun light backscattered or reflected to the instrument by the Earth's atmosphere or the surface. On its way between entering and leaving the top of the atmosphere, the observed light has been subject to various interactions between radiation and matter. The most relevant processes include scattering on air molecules and particles (aerosols or cloud particles), reflection at the Earth's surface or interaction with the upper layer of the ocean (see Fig. 2.5). In contrast to limb or occultation observations, atmospheric refraction can often be neglected for nadir viewing geometry.

a   Molecular Scattering

The most important molecular scattering process is elastic scattering, usually referred to as Rayleigh scattering. Rayleigh scattering is strongly wavelength dependent. The probability that a photon is scattered by a molecule increases as a function of the fourth power of its frequency. This results in the blue colour of the cloud-free sky. For this Rayleigh scattering, the probability distribution of the new directions of the scattered photons (defined as the phase function) depends on the degree of polarisation of the incident light as shown in Fig. 2.6. For unpolarised light such as that from the sun, scattering in forward or backward direction is twice as probable as scattering at $90°$. For linearly polarised electromagnetic radiation the probability of being scattered in directions parallel to the electric field vector is zero
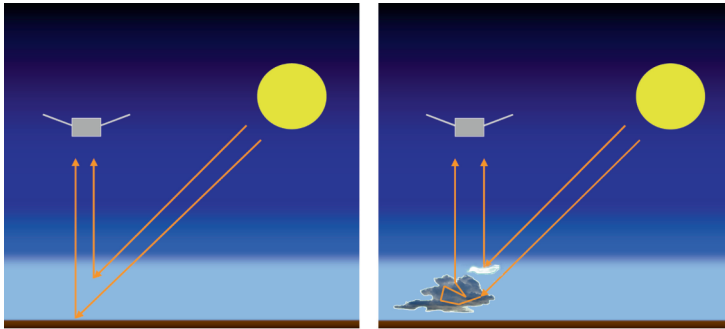
Fig. 2.5 The light received by a satellite instrument has undergone different interactions. In cloud-free scenes it is scattered by air molecules or reflected at the surface (*left*). In the presence of clouds (or aerosols) the light paths become further modified: scattering at high clouds can reduce the light paths, multiple scattering inside thick clouds can even enhance the light paths. Over bright surfaces, multiple scattering in the boundary layer can also be relevant under cloud free conditions (see Fig. 2.10).
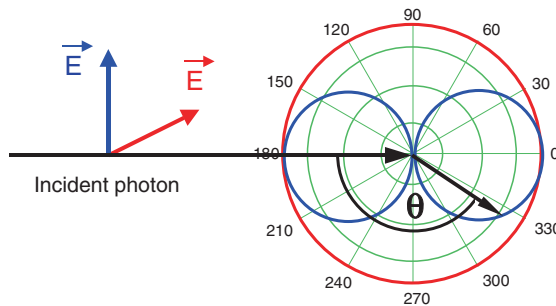

Fig. 2.6 Phase function for Rayleigh scattering. The vector of the electric field indicates the polarisation of the incident photon (*blue*: e-vector in the image plane; *red*: e-vector perpendicular to the image plane). The polar diagram indicates the probability distribution of the new photon direction after the Rayleigh scattering event (the angle θ describes scattering in the image plane). The length of the *arrow* indicates the scattering probability. For electromagnetic radiation with the e-vector perpendicular to the paper plane the scattering probability is independent of the scattering angle θ.

(see Fig. 2.6). Thus Rayleigh scattered light which is scattered at 90° is completely (linearly) polarised; this effect can be observed on clear days during sunset or sunrise, when looking at the zenith through a polariser. The phase function $P(\theta)$ for Rayleigh scattering of unpolarised light is described by:

$$P(\theta) = \frac{3}{4}[1 + \cos^2(\theta)]. \tag{2.17}$$

A small fraction (a few percent) of molecular scattering processes takes place as inelastic rotational Raman scattering. The associated wavelength shifts are in the

order of only a few nm, causing the Ring effect (see Section 2.2.3). Also the effect of vibrational Raman scattering on air molecules has been considered, but was found to be negligible at the accuracy level of current measurements. In contrast to Rayleigh scattering, the phase function for rotational Raman scattering depends only weakly on the scattering angle and the state of polarisation (Kattawar et al. 1981).

b   Particle Scattering

How atmospheric particles (aerosols or clouds) scatter electromagnetic radiation depends on their size, shape and composition. For spherical particles (e.g. liquid cloud droplets), their scattering properties are well described by Mie theory (Mie 1908; van de Hulst 1981). The scattering properties depend on the real and imaginary parts of the refractive index and on the particle size. With increasing particle size (usually expressed as size parameter $\alpha = 2\pi r/\lambda$), the asymmetry between the probability for backward and forward scattering increases (see Fig. 2.7). The bulk scattering properties of typical size distributions of aerosol and cloud droplets can be approximated by simplified functions, for example, the Henyey-Greenstein function (Henyey and Greenstein 1941). In contrast to spherical particles, the scattering properties of non-spherical particles (e.g. soot or dust particles or crystals in ice clouds) and particles having complex composition cannot be described by a comprehensive theory based on just a few input parameters as is the case for Mie theory. However, in many cases, the bulk scattering properties of such particle populations can be approximated by Mie theory.
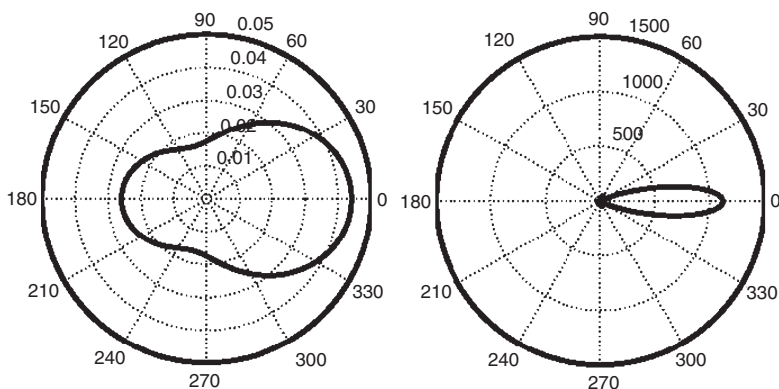

Fig. 2.7 Phase functions for Mie scattering (for refractive index of pure water). *Left*: for small droplet size ($\alpha = 1$); right for large droplet size ($\alpha = 5$). [adapted from (Sanghavi 2003)].

c Reflection and Absorption at the Surface

In addition to scattering from atmospheric constituents, reflection and absorption processes at the Earth's surface play an important role for satellite observations in nadir viewing geometry. The ratio of the reflected diffuse light to the incident irradiance defines the albedo, which usually depends on wavelength. The albedo depends on the characteristic of the incident light: the so called white and black sky albedo is defined for diffuse or directional incident light, respectively. The albedo ranges from zero (all photons are absorbed) to unity (all photons are reflected). The wavelength dependence of the surface albedo differs strongly over the globe (see Fig. 2.8). For most surface types (except snow or ice), the Earth's albedo in the UV/vis spectral range is quite low (between 2 and 30%). Towards the NIR the albedo over the continents increases for most surface types, whereas it decreases to very low values over the oceans. The highest surface albedo is found over snow and ice covered areas; increased reflectivity is also found in the case of sun glint over the ocean. The directional characteristic of surface reflection is described by the bi-directional reflection distribution function (BRDF); the reflected intensity depends on both the angles of the incident and reflected light. Often the BRDF is approximated by a Lambertian reflection characteristic (isotropic distribution of the reflected light, independent of the direction of the incident light). While some surface types (e.g. sand, snow, ice) are well described by this approximation, for many others (e.g. over vegetation, or for sun glint conditions over the ocean) more complex reflection functions are needed (see Fig. 2.9).
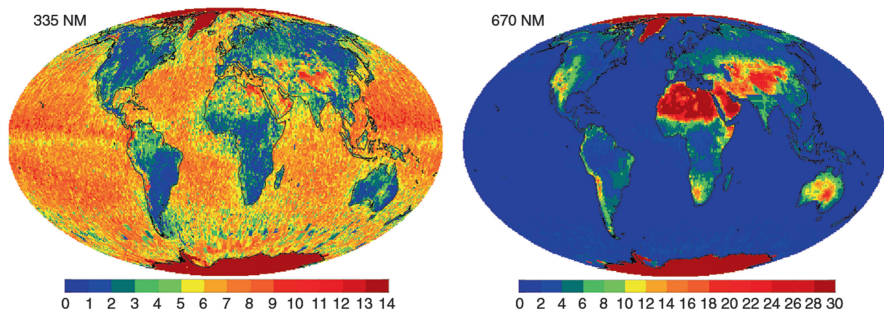

Fig. 2.8 Albedo of the Earth's surface at two wavelengths (*left* 335 nm, *right* 670 nm) [from Koelemeijer et al. (2003)].

d Interactions at the Ocean Surface

Part of the incident light is reflected directly at the ocean surface (by Fresnel reflection) causing sun glint, the intensity of which depends mainly on wind speed (surface roughness) and observation geometry (Cox and Munk 1954; 1956). The remaining part of the incident light can penetrate deeper into the water body. The
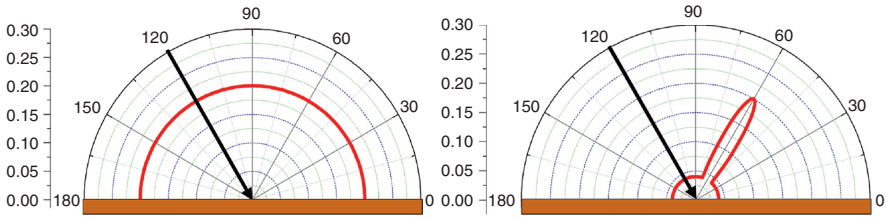
Fig. 2.9 Two examples for the angular dependency of the surface reflection. *Left*: for Lambertian reflection the probability of scattered light in any direction is constant (and independent on the angle of the incident light). *Right*: especially over the ocean, part of the light is reflected under the same angle as the incident ray (specular reflection). This effect is referred to as sun glitter or sun glint.

penetration depth depends strongly on the concentration of particles, in particular of phytoplankton which absorbs and scatters the light. In the presence of high phytoplankton concentrations (e.g. during algae blooms), the ocean albedo can be strongly enhanced in parts of the spectrum. Towards the near IR spectral range, the water absorption increases strongly and the penetration depth into the water body decreases; in these spectral regions the albedo of the oceans is especially low and strongly angle and surface state dependent, being 1% and less.

The incident photons are also scattered by water molecules. Besides elastic scattering, inelastic scattering, mainly due to vibrational Raman scattering, can also occur (see Section 2.2.3). The strongest signal of vibrational Raman scattering is typically found for oceanic regions with the lowest concentrations of particles, for which the penetration depth of the incident sun light is largest.

e   Molecular Absorption Processes

Satellite observations of atmospheric trace gases in the UV/vis and NIR spectral range are based on the spectral signatures of the absorption of molecules. Molecular absorption typically contains both broad and narrow spectral structures (within the sub-nm range, see Section 2.1.2). The latter can be easily identified and analysed in spectral retrieval processes (see Section 2.2.2).

For the correct interpretation of satellite observations, all the relevant processes discussed above have to be considered and included in the radiative transfer simulations.

Depending on wavelength, measurement conditions, and targeted quantity, the radiative transfer simulations might be simplified by omitting some of the processes discussed. For example, Raman scattering processes can often be neglected because of their small contribution to the total received light. In the NIR, the probability for Rayleigh scattering becomes so low that it can often be neglected.

2.3.2   Quantities Used for the Characterisation of the Measurement Sensitivity

a   The Total AMF

For most UV/vis/NIR retrievals, the basic result of the spectral analysis is the slant column density (*SCD*) (Eq. 2.2), the trace gas concentration integrated along the atmospheric light paths. Typically the *SCD* is converted into more universal quantities like the vertical trace gas column density, which is defined as the vertically integrated trace gas concentration (Eq. 2.3). The ratio between the *SCD* and *VCD* is referred to as the air mass factor (*AMF*):

$$AMF = \frac{SCD}{VCD}. \tag{2.18}$$

Only for a few viewing geometries, the *AMF* can be simply determined by geometric considerations. This is possible, for example, for nadir satellite observations made in the near IR where the probability of Rayleigh scattering is very small. For cloud free conditions, the observed light is then almost exclusively reflected by the surface and the elongation of the light path (with respect to the vertical path) can be approximated by:

$$AMF = \frac{1}{\cos(LOS)} + \frac{1}{\cos(SZA)}. \tag{2.19}$$

Here *LOS* denotes the line of sight angle of the instrument (defined with respect to the nadir direction), and *SZA* the solar zenith angle (defined with respect to the zenith direction). At solar zenith angles smaller than 70°, the geometric approximation can also be applied for nadir observations of stratospheric trace gases, even if they are made at visible and UV wavelengths. Since the air density in the stratosphere is low, almost all scattering events take place below the stratosphere, and the light paths through the stratospheric trace gas layers can be adequately described by simple geometry until the curvature of the atmosphere becomes relevant at low sun.

In contrast, for nadir satellite observations of tropospheric trace gases made at visible or UV wavelengths, due to Rayleigh scattering on air molecules the light paths in the tropospheric trace gas layers can become very complex. In such cases numerical radiative transfer simulations have to be performed for determining the *AMF*. The most complex light paths occur in the presence of clouds or strong aerosol loads. In such cases, even for observations in the near IR, radiative transfer simulations have to be performed.

Besides the dependence of the *AMF* on the *SZA* and *LOS* (see Eq. 2.19) the *AMF* usually depends on various other parameters, like the surface albedo, the wavelength,

the properties of aerosols and clouds, and the vertical distribution of the trace gas. For optically thick absorbers (the vertical optical thickness $\tau \gg 0$) they also become dependent on the trace gas *VCD* itself.

The *AMF* can be derived from radiative transfer simulations in various ways. One universal and often used procedure is based on the simulation of the radiance observed by the detector with or without the atmospheric trace gas of interest. According to the Beer-Lambert law the *SCD* can be expressed as:

$$SCD = \frac{1}{\sigma(\lambda)} \ln \frac{I'(\lambda)}{I(\lambda)} \tag{2.20}$$

here, I and I' denote the modelled radiances with and without the trace gas, respectively and $\sigma(\lambda)$ is the absorption cross-section. Using the definition of the *AMF*, Eq. 2.20 becomes:

$$AMF = \frac{\ln(I') - \ln(I)}{\sigma(\lambda) \cdot VCD} \tag{2.21}$$

VCD is the vertically integrated concentration of the trace gas as it was used as input of the radiative transfer simulations.

It is interesting to note that for weak absorbers the total *AMF* can be approximated by the "intensity weighted approximation" (Solomon et al. 1987; Slusser et al. 1996):

$$AMF = \frac{\sum_i AMF_i \cdot I_i}{\sum_i I_i} \tag{2.22}$$

Here the sum is taken over all light paths contributing to the measured signal. The AMF_i denote the geometrical path length weighted by the vertical profile of the trace gas, and I_i the radiance observed from light path i, respectively. The *AMF* determined using the intensity weighted approximation does not depend on the absorption of the target trace gas, but can depend on other atmospheric absorbers (e.g. an *AMF* determined for a NO_2 profile can depend on the optical depth of the atmospheric O_3 absorption).

The *AMF* as defined in Eqs. 2.18, 2.21, and 2.22, is usually referred to as "total" *AMF*, since it describes the sensitivity of the measurement for the complete atmospheric column density of the trace gas.

b   Box-AMF and Weighting Functions

In order to quantify the vertical dependence of the measurement sensitivity, it is useful to define a height-resolved partial *AMF* for specific atmospheric layers, the so called Box-*AMF* (or Block-*AMF*):

$$BAMF_i = \frac{\partial SCD}{\partial VCD_i} \qquad (2.23)$$

Here $BAMF_i$ denotes the Box-AMF for the atmospheric layer i, and VCD_i the partial vertical column density for layer i. If the absorber concentration ρ_i in layer i is assumed to be constant with altitude, Eq. 2.23 can be rewritten as:

$$BAMF_i = \frac{\partial SCD}{h_i \cdot \partial \rho_i} \qquad (2.24)$$

where h_i denotes the vertical extension of layer i.

The Box-AMF definition can also be related to the measured radiance. Using the relations of Eq. 2.20, it follows:

$$BAMF_i = \frac{1}{\sigma \cdot h_i} \cdot \frac{\partial (\ln I/I')}{\partial \rho_i} \qquad (2.25)$$

Note that in some retrieval algorithms also the derivative of the intensity is calculated (see also Section 2.2.4). The weighting functions, WF, are defined as:

$$WF_i = \frac{\partial I}{\sigma \cdot h_i \cdot \partial \rho_i} \qquad (2.26)$$

As can be seen, it is closely related to the Box-AMF in that it only describes changes in intensity and not in slant column density.

An example for the vertical variation of Box-AMFs for satellite observations in nadir viewing geometry is shown in Fig. 2.10. For long wavelengths the height dependence is weak, because most photons are reflected at the surface. For shorter wavelengths the influence of Rayleigh scattering becomes more important; for the troposphere, this leads to a decreased sensitivity at low albedo and increased sensitivity for high albedo (due to multiple scattering).

In Fig. 2.11 Box-AMFs for satellite nadir observations are shown for situations when clouds and aerosols are present.

Eqs. 2.23–2.25 are valid for all atmospheric situations, also including observations of optically thick absorbers ($\tau \gg 0$) like O_3 in the UV spectral range. However, with increasing optical thickness, the respective Box-AMFs also become dependent on the absolute value of the trace gas concentration in the different layers. In general, with increasing optical thickness, the Box-AMFs become smaller, indicating decreasing measurement sensitivity.

Fortunately, for most atmospheric species the optical density in the UV/vis/NIR spectral range is small ($\tau \ll 1$). For these weak absorbers the Box-AMFs become essentially independent of the absolute value of the trace gas concentration, and several simplifications can be made.
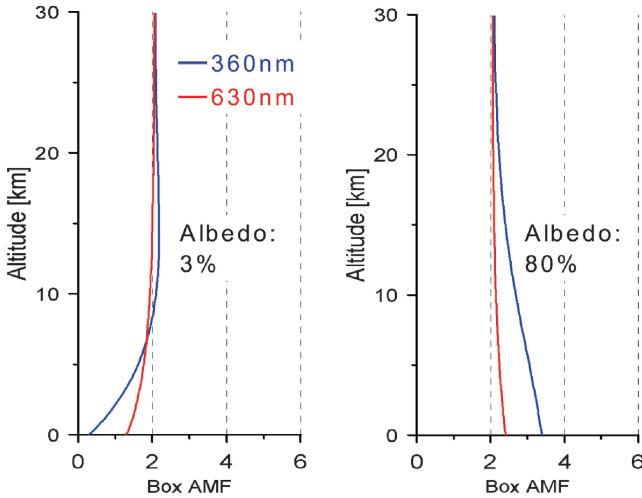
Fig. 2.10 Height-dependence of the sensitivity of satellite observations in nadir viewing geometry, expressed as Box-AMFs. For large wavelengths, only a weak height dependence is found. For shorter wavelengths, the Box-AMFs decrease towards the surface for low albedo (*left panel*) and increase for high albedo (*right panel*). SZA was chosen as 0°.
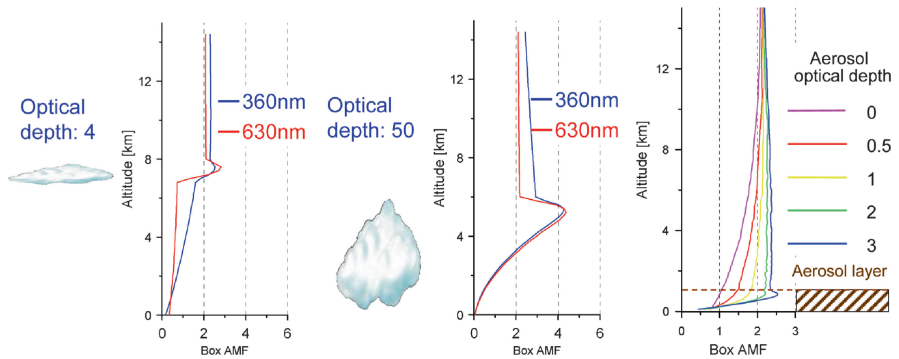

Fig. 2.11 Height-dependence of the sensitivity of satellite observations in nadir viewing geometry in the presence of clouds and aerosols (expressed as Box-AMFs). High, thin clouds mainly shield trace gases below the cloud (*left*). Thick clouds increase the sensitivity in the upper layers of the clouds and decrease the sensitivity towards the surface (*centre*). The effect of near surface aerosols depends on their optical thickness, phase function, and their single scattering albedo. Non-absorbing aerosols can substantially increase the sensitivity (*right*). Surface albedo and SZA were chosen to be 5% and 0°, respectively.

First, the Box-*AMF* can be simply determined by averaging the geometrical path lengths of the individual light paths through layer i, weighted by their intensities (similar to Eq. 2.22 for the total *AMF*):

$$BAMF_i = \frac{\sum_j l_{i,j} \cdot I_{i,j}}{h \cdot \sum_j I_{i,j}} \tag{2.27}$$

Here $l_{i,j}$ and $I_{i,j}$ describe the length and intensity of light path j through layer i, and h the vertical extension of the layer. In addition, for optically thin absorbers for which the light path does not depend on absorber concentration, the Box-*AMF* can simply be expressed as the ratio of the partial SCD_i and the partial VCD_i of an atmospheric layer i:

$$BAMF_i = \frac{SCD_i}{VCD_i} \qquad (2.28)$$

From this follows the most important simplification, which is that the total *AMF* (as defined in Eqs. 2.28, 2.21 and 2.22) can be directly determined by combining the height profiles of Box-*AMF*s and the (relative) trace gas concentration:

$$AMF = \frac{SCD}{VCD} = \frac{\sum_{i=0}^{TOA} SCD_i}{VCD} = \frac{\sum_{i=0}^{TOA} BAMF_i \cdot VCD_i}{VCD} = \sum_{i=0}^{TOA} BAMF_i \cdot \frac{VCD_i}{VCD} \qquad (2.29)$$

Here VCD_i/VCD describes the relative trace gas concentration profile. Sometimes it is also referred to as shape factor (Palmer et al. 2001).

With this formulation, it becomes possible to separate completely the radiative transfer modelling from the assumptions made for the vertical trace gas distribution. Accordingly, different sets of Box-*AMF*s (e.g. for various aerosol and cloud profiles) can be pre-calculated and stored in look-up tables. By applying Eq. 2.29, the total *AMF* for arbitrary profile shapes can be easily calculated. This procedure is particularly convenient if the assumptions on the relative profile shape change (e.g. after new measurements or model results on the vertical trace gas distributions have become available) or if a large number of different airmass factors have to be calculated as is the case for satellite observations.

Eq. 2.29 is strictly valid only for weak absorbers. Nevertheless, if it is applied for moderate absorbers, the resulting errors are usually small, and can in most cases be neglected compared to other uncertainties (see Section 2.5).

c   Averaging Kernels

The knowledge of the height dependence of the measurement sensitivity is crucial for the correct interpretation of individual satellite measurements. In extreme cases, for example, in the presence of thick clouds, the satellite becomes almost blind for trace gases located below the cloud (see Figs. 2.5 and 2.11), and a low value of the retrieved trace gas *SCD* does not necessarily indicate a low trace gas concentration in the atmosphere. The height dependent measurement sensitivity has in particular to be considered if satellite observations are compared to other data sets (e.g. other measurements or model results, in the following referred to as "collocated data

sets"). There are two basic ways to consider the height dependent sensitivity in such comparisons.

(a) The first possibility is to simulate the trace gas *SCD* as measured by the satellite based on the collocated data set. This can be achieved by calculating the *AMF* according to the trace gas profile of the collocated data set. Applying Eq. 2.18 then yields the *SCD* which can be compared to the *SCD* retrieved from the satellite measurement. For weak absorbers, instead of Eq. 2.28, the Box-*AMF* concept can be applied (Eq. 2.29):

$$SCD = \sum_{i=0}^{TOA} SCD_i = \sum_{i=0}^{TOA} BAMF_i \cdot VCD_i \qquad (2.30)$$

The advantage of this procedure is that the Box-*AMF* can be calculated completely independently from the collocated data set.

(b) The second possibility for the comparison to a collocated data set is to convert the *SCD* obtained from the satellite observation first into a trace gas *VCD* using an (total) *AMF* (according to Eq. 2.18). For the simulation of the *AMF* a (relative) vertical profile shape of the absorber has to be assumed.

By dividing the Box-*AMF*s by the total *AMF*, so called column averaging kernels are determined (Eskes and Boersma 2003) (see Fig. 2.12):
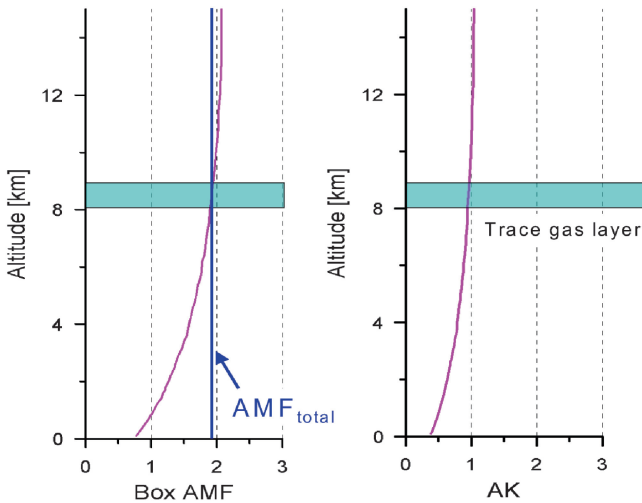
$$AK_i = \frac{BAMF_i}{AMF} \qquad (2.31)$$

Fig. 2.12 Column averaging kernels (*right*) can be easily derived by dividing the box-AMFs (*left*) by the total AMF for an assumed profile. In this case the total AMF is 1.9 according to a trace gas layer located between 8 and 9 km altitude. Surface albedo and SZA were chosen to be 5% and 0°.

The column averaging kernels provide information about how the retrieved *VCD* changes for a given change of the absorber concentration at a certain altitude range. It can be used to convert the trace gas profile of a collocated data set to the VCD^{instr} defined as the vertical column density which the retrieval should have produced for the collocated profile:

$$VCD^{instr} = \sum_{i=0}^{TOA} AK_i \cdot VCD_i \tag{2.32}$$

This quantity VCD^{instr} can be directly compared to that determined from the satellite observation. Here it is interesting to note that the *VCD* (both measured and simulated) might differ from the true atmospheric *VCD*, if the assumed (relative) profile differs from the true profile. Nevertheless, the comparison between measured and simulated trace gas *VCD* is not affected by this because for both quantities the same (potentially wrong) assumptions are made.

Mathematically, both ways to compare the satellite data to collocated data sets are equivalent. The choice between the two possibilities depends on the technical capabilities for the processing of the involved data sets and the objectives of the study. The comparison of *VCD*s (instead of *SCD*s) has the advantage that the trace gas fields are expressed in a more unified and intuitive way. Thus errors might be more easily identified.

In general, it should be noted that if disagreement between the simulated quantity (either *SCD* or *VCD*) and measured quantity is found, a straight forward interpretation is possible: one can then simply conclude that the data sets do not agree. In the case of agreement (at least within certain limits), the actual agreement of both data sets is only one (usually very probable) possibility. However, since various trace gas profiles can result in the same *SCD* (or *VCD*), also a wrong profile of the collocated data set might yield the same *SCD* (or *VCD*) as measured by the satellite.

d   2-D and 3-D Box-AMF

The Box-*AMF* concept introduced in Eq. 2.23 can be directly extended to two or three dimensions. For that purpose, Eq. 2.25 has to be modified:

$$BAMF_{i,j,k} = \frac{1}{\sigma \cdot h_i} \cdot \frac{\partial (\ln I/I')}{\partial \rho_{i,j,k}} = \frac{\partial SCD}{\partial VCD_{i,j,k}} \tag{2.33}$$

Here, like Eq. 2.25, the index i describes the vertical dimension. In addition, the height layers are also separated in distinct boxes in the two horizontal dimensions; they are described by the indices j and k. The three-dimensional Box-*AMF*s describe the dependence of the measured total SCD on changes in the concentration (or partial *VCD*) of box i, j, k.

Like the one-dimensional Box-*AMF* concept, also the multi-dimensional Box-*AMF*s can be used for the comparison of the satellite observations to collocated data sets.

The *SCD* measured by the satellite can be expressed by a collocated 3-dimensional data set:

$$SCD = \sum_{i,j,k} BAMF_{i,j,k} \cdot VCD_{i,j,k} = \sum_{i,j,k} BAMF_{i,j,k} \cdot h_i \cdot \rho_{i,j,k} \qquad (2.34)$$

In this way, the effect of 3-dimensional gradients of trace gases (and aerosols or clouds) inside a satellite ground pixel can also be investigated. This could be relevant around pollution hot-spots or in coastal regions with large spatial variability.

2.3.3   Important Input Data

Depending on the trace gas of interest, information about the various input data is required for the radiative transfer simulations in addition to the settings on viewing geometry and solar position. In contrast to stratospheric absorbers, the radiative transfer simulations for tropospheric trace gases are especially sensitive to the influence of the surface albedo, surface elevation, tropospheric aerosols, clouds, and the vertical trace gas profile. Furthermore, information on the profiles of temperature and pressure is required, but their influence on the radiative transfer simulations is quite weak.

Because of the large ground pixel size of many satellite instruments, horizontal gradients of trace gases, aerosols, clouds and the surface properties can also become important.

Information on several of these parameters is in general difficult to obtain, in particular at the high spatial resolution needed for recent satellite sensors. Most critical are input data on the vertical profiles of the trace gas concentration as well as the aerosol and cloud properties. As input data, independent information, e.g. from simultaneous observations of the cloud and aerosol properties, is often used. Information on the trace gas vertical profile can be obtained from collocated measurements (e.g. from aircraft) or model simulations of the atmospheric chemistry and transport. Also, standardised average profiles or proxy-information, such as the boundary layer height are sometimes used.

Considering their high relevance and limited availability, the largest sources of uncertainty for tropospheric radiative transfer simulations are caused by the influence of the vertical profiles of the trace gas concentration as well as cloud and aerosol properties.

Information on the various input data is summarised in Table 2.2.

As mentioned above, the impact of the *a priori* data on the derived quantities is sometimes large.

Table 2.2 Input information used for radiative transfer simulations of tropospheric trace gases

Input data	Importance	Typically used	Source of information
Trace gas profile	High	Yes	Independent information, e.g., from atmospheric models or general assumptions
Cloud properties	High	Yes	Simultaneous measurements, e.g., cloud fraction and cloud top height
Aerosol properties	High	No	General assumptions, atmospheric models, potentially also simultaneous measurements
Surface albedo	High	Yes	Climatologies, e.g., created from the same satellite instrument, sometimes also retrieved from the measurements
Surface elevation	Medium	No	Databases
Pressure and temperature profile	Low	Yes	Standard profiles
Solar zenith angle	Medium	Yes	Measurement description
Line of sight angle	Medium	No	Measurement description
Relative azimuth angle	Medium	No	Measurement description
Horizontal gradients of clouds, aerosols, trace gases, surface albedo and elevation	Potentially high	No	Data bases, atmospheric models, general assumptions

As discussed in Section 2.3.2, in comparisons with model data, this problem of dependence on *a priori* data can be addressed by either applying the averaging kernels of the measurements to the model data or by converting model profiles to slant column densities.

2.3.4 Overview of Existing Radiative Transfer Models

The direct output of radiative transfer models is usually the radiance measured by a specified detector under defined atmospheric properties and for a given solar position. From the modelled radiance, also other quantities, e.g. air mass factors, can be obtained subsequently (see Eqs. 2.20–2.22, 2.25, 2.26 and 2.33). To describe the observed radiance at a detector, the radiative transfer equation (see also Chapter 1) has to be solved.

$$
\frac{dI(\lambda, \varphi, \vartheta)}{ds} = -[\sigma_S(\lambda) + \sigma_A(\lambda)] \cdot \rho \cdot I(\lambda, \varphi, \vartheta) + \sigma_A(\lambda) \cdot \rho \cdot B(\lambda, T)
$$
$$
+ \int_{4\pi} \frac{d\sigma_s}{d\Omega}(\lambda, \varphi, \vartheta, \varphi', \vartheta') \cdot \rho \cdot I(\lambda, \varphi', \vartheta') d\Omega \qquad (2.35)
$$

Here $I(\lambda, \varphi, \vartheta)$ describes the intensity along the line of sight (denoted by the two angles φ, ϑ); σ_S and σ_A denote the scattering and absorption cross-section, respectively. ρ is the number density of the molecule and $B(\lambda, T)$ describes the black body radiation. The last term contains the light which is scattered from any direction into the line of sight. The probability for scattering from the original direction φ', ϑ' into the line of sight is described by the differential scattering cross-section $d\sigma_s/d\Omega$ $(\lambda, \varphi, \vartheta, \varphi', \vartheta')$, also referred to as a phase function, see Section 2.3.1. In the real atmosphere, this equation has to be expanded to include all species present with their respective densities and absorption and scattering cross-sections. For observations in the UV, visible and near-IR spectral range, the thermal emission term can usually be neglected as it is very small at atmospheric temperatures.

For the purposes of UV/vis/NIR retrievals, the radiative transfer equation can be solved using different methods with specific advantages and disadvantages. Early models often used so called two stream approaches, which assume horizontally homogenous conditions and simulate the integrated upward and downward radiation fluxes (Meador and Weaver 1980). However, such models are usually applied to plane parallel atmospheres and are not able to reproduce the angular dependence of the radiation field. Today, usually more sophisticated models are used, which overcome these limitations (Wendisch and Yang 2010; Perliski and Solomon 1993; Sarkissian et al. 1995; Hendrick et al. 2006; Wagner et al. 2007b).

Analytical models usually describe the direct, single scattered and multiply scattered contributions separately. Such models are in general very fast, but analytical solutions can only be found for single scattering or for plane parallel geometry. To describe adequately measurements at large solar zenith angles, or almost horizontal viewing directions, full multiple scattering, approximations and iterative approaches have to be applied.

Another widely used method is based on the Monte-Carlo technique, which simulates individual photon paths contributing to the measured signal at the detector. From a modelled photon path ensemble, the observed radiance, and also statistical quantities (like the average scattering frequency, etc.) can be determined. To achieve high accuracy, however, a large number of photon paths have to be modelled, which can become very time-consuming. Monte-Carlo models offer the most realistic description of the relevant processes and the boundary conditions like the Earth's curvature and topography. An overview on various methods to simulate the atmospheric radiative transfer can be found in Wendisch and Yang (2010).

Depending on the complexity of the considered situation and on the required accuracy, several simplifications with respect to the full range of interaction processes can be made. These simplifications usually lead to higher computational speed. They include the following aspects.

(a) Most radiative transfer models do not include a correct treatment of polarisation. While the incoming solar light is unpolarised, scattering and reflection processes can cause the observed light to be polarised (depending on the viewing geometry). For most atmospheric applications, only linear polarisation

has to be considered. If the atmospheric radiative transfer is described by scalar models, in specific cases, systematic errors can occur. For most situations, these errors are below a few percent (Mishchenko et al. 1994).

(b) Many models only describe first order scattering processes especially in stratospheric applications. Since the air density in the stratosphere is low, the probability for multiple scattering is usually rather small and neglecting higher scattering orders leads to small errors (up to a few percent). Single scattering models are very efficient and were mainly used in early studies (Solomon et al. 1987; Perliski and Solomon 1993). Today, due to the increased computer power, for stratospheric applications, multiple scattering models are usually also used. For the simulation of satellite observations of tropospheric trace gases, multiple scattering has to be included due to the increased air density and the effects of clouds and aerosols.

(c) For many applications, the Earth's curvature (and also refraction) is neglected, since plane parallel models can be operated much more efficiently. However for situations with large SZA (>85°) and/or almost horizontal viewing direction (e.g. in limb viewing geometry) neglecting the Earth's curvature leads to considerable errors (Wagner et al. 2007b).

(d) Most models do not consider Raman scattering. Since the probability for Raman scattering is low (e.g. a few percent of molecular scattering is rotational Raman scattering), the resulting error for the modelled radiance is usually negligible. However, if the atmospheric Ring effect is simulated explicitly, Raman scattering has to be included. Such model simulations are usually very time-consuming because the scattering contributions from many wavelengths have to be considered simultaneously (Joiner et al. 1995; Joiner and Bhartia 1995).

2.4   Separation of Tropospheric and Stratospheric Signals

Measurements in the UV/visible spectral range usually do not contain intrinsic information on the vertical distribution of the absorber of interest. This is in contrast to data taken in the IR and microwave regions (see Chapters 3 and 4), where line broadening and temperature dependence can be used to invert vertical atmospheric profiles. While some absorbers have the potential for direct retrieval of altitude information, as will be discussed at the end of this section, current algorithms do not use these possibilities. Instead, they rely on the use of assumptions and external information to extract the tropospheric part of the measured signal.

The signal received at the satellite results from scattering in the atmosphere by molecules, cloud and aerosol particles, and reflection on the surface. Therefore, both absorptions in the troposphere and in the stratosphere contribute to the slant column density *SCD* derived from the measurements. For some species such as HCHO the stratospheric concentrations are so small, that one can safely assume that the observed signal is purely tropospheric. However, for most other species, notably

O_3, NO_2, and BrO, the stratospheric column densities are appreciable and in many cases larger than the tropospheric column densities. This is further aggravated by the fact that the light path and thus the total absorption usually are larger in the stratosphere than in the troposphere. Therefore, an accurate method is needed to estimate the stratospheric column density before the tropospheric part can be determined (Fig. 2.13).
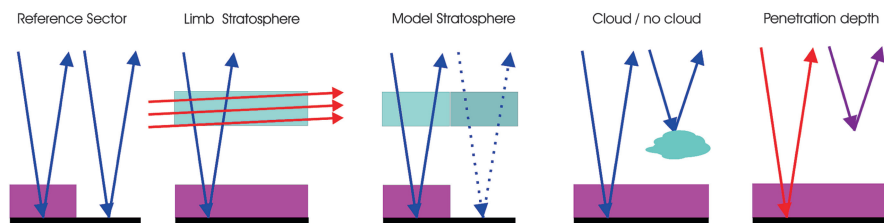

Fig. 2.13 Schematic overview over some methods to separate tropospheric and stratospheric signals. From *left* to *right*: using a measurement over clean regions, independent measurements of the stratospheric column density, (assimilated) model values for the stratosphere, cloud slicing or measurements at different wavelengths having different penetration depths.

2.4.1   Stratospheric Measurement Methods

For O_3, this problem has been addressed by using measurements from two different instruments – TOMS, from which total atmospheric column densities of O_3 can be retrieved, and SAGE and SBUV, which provide stratospheric profiles (Fishman and Larsen 1987). By subtracting the stratospheric column density derived from the profile measurements from the total column density, the tropospheric part can be obtained. If this method is applied to long-term averages, climatological tropospheric O_3 fields can be determined which are in good agreement with independent measurements. The approach relies on several assumptions, in particular that temporal variations in the tropospheric and stratospheric fields are not correlated and therefore independent averaging can be applied. Also, the weighting of the tropospheric signals in the total column densities has to be considered as the sensitivity of the measurements decreases towards the surface (see Section 2.3.2). The method also requires very accurate measurements as only about 10% of the total O_3 column density is located in the troposphere, and therefore a 5% error on the stratospheric column density will result in an error of approximately 45% on the tropospheric amount. The method has been extended to other instruments, e.g. OMI and the Microwave Limb Sounder (MLS) on Aura (Schoeberl et al. 2007), which have nearly coincident measurements and therefore, in combination with trajectory calculations, can be used to retrieve daily tropospheric O_3 maps.

Another variant of the idea to use integrated stratospheric profiles to extract the tropospheric amount from total column information is the limb-nadir matching which can be applied with SCIAMACHY measurements (Bovensmann et al. 1999; Sierk et al. 2006; Sioris et al. 2004; Beirle et al. 2010). The latter instrument is unique in that it takes two measurements of the same air mass within several minutes – first a limb scan providing the stratospheric profile and 7 min later a nadir measurement of the total column density. These data provide optimum coincidence in space and time and, in principle, can be used not only for O_3 but also BrO and NO_2. A complication of the limb-nadir measurements is the reduced sensitivity of limb observations to the lower stratosphere, in particular in mid and high latitudes which results in larger uncertainties of the stratospheric column densities.

2.4.2 Residual Methods

Another approach often used to estimate the stratospheric contribution to the measurements is based on assumptions on the spatial distribution of the strato-spheric species. Stratospheric O_3 in the tropics, for example, can be assumed to vary mainly with latitude and much less with longitude. Assuming that the tropospheric ozone burden in a clean region, e.g. over the Pacific, is small, then one can compute the tropospheric excess column density as a function of latitude for all longitudes relative to the "clean air sector". For O_3, this is only applicable in the tropics and has to be refined further by accounting for stratospheric wave patterns (Hudson and Thompson 1998). For NO_2, the method can even be extended to mid-latitudes with good results, at least for instruments in sun-synchronous orbits where the diurnal photochemistry does not come into play (Richter and Burrows 2002; Martin et al. 2002). Because of the short lifetime of NO_2, the assumption of low tropospheric column densities over the Pacific is usually fulfilled but some errors are introduced from dynamical variations in NO_2, in particular those linked to the polar vortex.

An extension of the residual method for NO_2 has been developed for the GOME and OMI instruments, where a 2-dimensional smooth field is fitted through the global total column density measurements after masking out regions with known tropospheric sources (Leue et al. 2001; Bucsela et al. 2006). With this approach, dynamical features are also compensated for, but some large scale tropospheric signals could be potentially removed.

2.4.3 Model Method

As global 3D-CTMs simulate stratospheric fields of many absorbers with good accuracy, one can also use model results to remove the stratospheric component of the signal. To compensate biases in both model and measurements, the model

results are usually scaled to the measurements over the reference region (Richter et al. 2005) or assimilation techniques are applied (Boersma et al. 2007). For example, the satellite-derived total column densities can be assimilated directly applying specific weighting to reduce the impact of tropospheric contamination (Boersma et al. 2007). These methods further improve the accuracy of the stratospheric correction in particular in the vicinity of the polar vortex. However, as one cannot separate model measurement offsets resulting from inaccuracies in model or measurement, and those resulting from true tropospheric signals, this approach also runs the risk of removing large scale tropospheric signals in the assimilation process.

2.4.4   Cloud Slicing method

In regions where clouds have varying cloud top altitudes sometimes reaching the tropopause, a method called cloud slicing can be used to separate troposphere and stratosphere and in addition to derive vertical profiles within the troposphere (Ziemke et al. 1998; 2001). The method relies on the shielding effect of optically thick clouds (see Section 2.3.2) and assumes that the trace gas is distributed homogeneously, either within a scene with different cloud top heights or over time if measurements from different days are combined. This approach has been used for O_3 data mainly limited to the tropics. Radiative transfer effects within the clouds can have an impact on the results, as well as changes in absorber concentration by vertical redistribution in updrafts, changes in photolysis frequencies, wet scavenging or lightning production introducing uncertainty in the retrieved tropospheric column densities. A method based on a similar idea compares measurements over high mountains with those from low altitude areas in the vicinity (Jiang and Yung 1996).

2.4.5   Other Possible Approaches

Ideally, the stratospheric and tropospheric contributions should be separated solely by using information from the individual measurements. For O_3 in the stratosphere, combination of measurements at different wavelengths provides information on the vertical distribution as the penetration depth of photons into the atmosphere decreases with increasing O_3 absorption towards shorter wavelengths. In principle, use of the Chappuis bands for a total column density with good weighting of the tropospheric contribution in combination with a UV retrieval should provide some information on the tropospheric part (Chance et al. 1997). However, this has not so far been realised, mainly because of interference of chlorophyll and surface absorptions in the Chappuis window (see Section 2.5.3). Using UV measurements only, a separation of troposphere and stratosphere has been achieved for O_3 (Hoogen et al.

1999; Liu et al. 2005) and even more vertical information could be retrieved for strong volcanic SO_2 signals (Yang et al. 2009).

A similar approach can be applied to NO_2 using the variation of vertical sensitivity from 360 to 500 nm which is mainly determined by Rayleigh scattering and surface albedo changes. While this approach has been demonstrated in principle (Richter and Burrows 2000) it has relatively large uncertainties from surface albedo and aerosol and cloud effects. Another source of information on the vertical distribution could be polarisation (Hasekamp and Landgraf 2002) but this needs polarised measurements with high spectral resolution which are not available so far. Potentially, the temperature dependence of absorption cross-sections can also be used to derive vertical information by taking advantage of the temperature contrast between troposphere and stratosphere. The temperature dependence of the absorption is already used in stratospheric O_3 profile retrieval but the resulting signal is small for the troposphere and has not yet been used.

A completely different approach relies on the use of neural networks which are trained on large sets of satellite data in combination with independent measurements. Besides their high efficiency in processing large amounts of data, the main advantages of neural networks are that they can be applied even in cases with insufficient knowledge or too high complexity of the measurement process or instrument performance. However, it should be noted that neural networks usually fail if the measurement conditions (or instrument performance) are outside the range which was used for the training (e.g. due to instrument degradation). For O_3, good consistency of the tropospheric column densities extracted with this method has been demonstrated (Müller et al. 2003).

2.5   Uncertainties in UV/vis/NIR Satellite Measurements

There are several sources of error which need to be taken into account when interpreting satellite measurements of tropospheric composition. Some of the errors are random and can be reduced by averaging, while others are systematic and more difficult to quantify.

The fundamental uncertainty of any remote sensing measurement is linked to the signal strength or the number of photons collected in a single measurement and the associated probability distribution. For the ideal situation where there is no instrument noise, the photon shot noise is the ultimate limit for the noise of the radiance signal. The ratio of this noise to the signal determines the minimum observable optical thickness and thus the minimum detectable *SCD*. For real data, retrievals have to deal with additional error sources, including instrument noise, uncertainties in spectroscopic parameters, imperfect knowledge of the atmospheric light path and errors in the *a priori* assumptions used. Many of the uncertainties have been discussed in the literature (for NO_2 in (Boersma et al. 2004; Martin et al. 2002; van Noije et al. 2006) and references therein). The most relevant are summarised in Table 2.3 and will be briefly discussed below.

Table 2.3 Error sources in some quantities in UV/vis retrievals of tropospheric species

Radiance	Slant column density	Tropospheric slant column density	Tropospheric vertical column density
Photon shot noise	Cross-sections	Stratospheric correction	Surface albedo
Detector noise	Temperature dependence		Cloud height and fraction
Stray-light	Spectral interference		Vertical absorber distribution
Instrument throughput			Aerosol loading
Polarisation sensitivity			

2.5.1 *Instrument Noise and Stray Light*

The noise of the measured radiance for real instruments comprises the photon shot noise, the noise from the detector dark signal and the readout noise. For measurements over bright scenes, e.g. clouds, ice, or desert, the signal detected by a nadir looking instrument like GOME or SCIAMACHY is usually large and the total noise is dominated by photon shot noise for cooled detectors. However, over dark surfaces, or at short integration times (good spatial resolution), the instrument noise can become a significant contribution to the total noise. This is particularly true in the NIR part of the spectrum, where molecular scattering is less efficient and very low signals are measured, for example, over the ocean. In addition, detectors still suffer from much larger dark signals than in the UV/vis. For most instruments, measurement noise is strongly enhanced in the region of the Southern Atlantic Anomaly where an anomaly in the Earth's magnetic field leads to increased influx of radiation and particles on the instrument detectors and their electronics.

At very short integration times, the sequential readout of the detectors can no longer be neglected causing the spatial footprint of the measurements to vary with wavelength. Over strongly inhomogeneous scenes, e.g. broken clouds, this can lead to aliasing noise in the spectra as changes in intensity related to spatial patterns are misinterpreted as changes in intensity with wavelength. Future instruments could remove this source of error by using improved readout electronics.

In particular for the UV part of the spectrum, stray light generated within the instrument is a potential problem because the light intensity reaching the instrument is many orders of magnitude higher at longer wavelengths than in the UV. Even a small fraction of visible photons scattered to the UV part of the detector can be significant at the low signals found there, leading to distortion of the spectra and underestimation of absorption. Similarly, fluctuations in the dark signal of the detector or the electronic offset added prior to readout can be relevant at low signals if not accounted for. For this reason all instruments measuring in the UV attempt to minimize the stray-light within the instrument.

Photon noise, instrument noise and aliasing noise are statistical error sources which are reduced by averaging of measurements in space or time and therefore affect the precision but not the accuracy of the measurements. Instrumental stray-light in contrast is a systematic error, which reduces the absorption signals and cannot be offset by averaging.

2.5.2   Spectroscopic Uncertainties and Instrument Slit Width

The retrieval of the amounts and distributions of atmospheric trace gases in the UV/visible spectral range is based on molecular absorption spectroscopy. The uncertainty on the absorption cross-section of the trace gas of interest therefore directly translates to an uncertainty of the tropospheric amounts retrieved for the species: this is usually in the range of several percent. In addition to the knowledge of the absolute trace-gas cross section, any uncertainty in the knowledge of the detailed wavelength dependence of the absorption cross-section is relevant for DOAS or equivalent retrieval algorithms. As typical satellite instruments observing in the UV do not resolve the full spectral details caused by atomic and molecular absorption within the sun and the Earth's atmosphere, the slit function of the instrument must be well characterised as the reference spectra must be convolved to the instrument resolution. Any inaccuracy in this convolution results in additional error sources. Similarly for measurements by instruments at discrete wavelengths, the exact band pass of each measurement point and its stability over time are key aspects.

Many of the absorption cross-sections exhibit a temperature dependence which has to be characterised in the laboratory. However, even if the temperature dependence of the cross-section is perfectly known, the atmospheric temperature of the absorbing species is often not known to sufficiently high accuracy, introducing a further potential source of systematic error.

Spectroscopic errors are non-random relative errors and cannot be reduced by averaging. They are best assessed by validation of retrieval results with independent measurements.

2.5.3   Spectral Interference

Arguably the most complex source of uncertainties for the DOAS and related retrieval techniques arises from spectral interference. This is where spectral structures are erroneously attributed to absorption of one absorber although they originate with another absorber, with the instrumental features or with the wavelength dependence of surface reflectance. Ideally in a given spectral window the spectra of the absorbing and scattering features are all orthogonal to one another and have no correlation. However, as result of the spectral correlation between the signatures of

different effects, spectral interference occurs. This is observed even for synthetic data with perfect spectra, but is obviously a larger source of uncertainty in real measurements. This increased sensitivity to correlation is the result of errors in the absorption cross-sections used, the slit function and the limited spectral resolution.

In most spectral windows used for retrieval, more than one species contribute to the observed absorption signal and, for weak absorbers, the interfering signals are often more than an order of magnitude larger than the quantity of interest. In addition to other atmospheric absorbers, inelastic scattering in the atmosphere (Ring effect), surface spectral reflectance, and wavelength dependent instrument transmission changes can also interfere with the retrieval of absorption signals. The usual approach, taken to minimise the false identification of molecular absorption, is to select spectral regions where the correlation between the absorption cross-section of the target molecule and that of other molecules is a minimum and the absorptions of the interfering species are small. The remaining impact is then accounted for by including the absorbers in the least squares fit. The same approach is taken for instrumental effects, which are not fully compensated through calibration by introducing appropriate pseudo absorbers in the retrieval.

For instruments observing light at discrete wavelengths, the problem of spectral interference is more severe as usually insufficient information is retrieved from the measurements to separate the effect of different absorbers.

The effect of spectral interference on the retrieved tropospheric products must be quantified for each spectral window selected and the particular instrument, having its unique instrumental characteristics. The best way to assess the impact of spectral interferences is to perform sensitivity studies by varying the analysis properties such as the wavelength range. In most cases, the errors are systematic and cannot be fully removed by averaging.

2.5.4   *Light Path Uncertainties*

Besides errors associated with the spectroscopic part of the retrieval, the imperfect knowledge of the light path through the atmosphere also introduces uncertainties in the determination of total *VCD*s, tropospheric *VCD*s or vertical profiles of trace gases. Radiative transfer models, when provided with accurate input for the atmospheric and surface conditions, can simulate the radiation field and the *AMF* with high accuracy. However, some of the important input parameters are usually not known perfectly (see Section 2.3.3). This can lead to large uncertainties in individual measurements.

As the measurements of UV/vis radiance beyond ~320 nm contain little or no information on the vertical distribution of the absorbers, this information has to be taken from other measurements, climatologies or atmospheric models. In combination with the altitude dependence of the measurement sensitivity, this is an intrinsic uncertainty for the determination of *VCD*s and tropospheric *VCD*s. All the parameters influencing the altitude dependence of the sensitivity have to be accounted

for in the radiative transfer model, including surface spectral reflectance, aerosol load and distribution and clouds. All of these parameters vary in space and time, for example as vegetation changes, ice melts or sand storms develop and terminate.

The presence of clouds has a particularly important potential to reduce the sensitivity of space-borne UV/vis measurements to absorptions in the boundary layer to very low values by their shielding properties. As they are bright compared to the surface, even relatively small cloud fractions within a ground scene can have a significant impact on the measurements. This is because the absorption is weighted by the photon flux from the different parts of the scene.

Current approaches to account for cloud effects rely mostly on the retrieval of cloud properties from the measurements themselves by analysing the signals of absorbers with well known vertical distributions such as O_2 (Kuze and Chance 1994; Koelemeijer et al. 2001; Rozanov and Kokhanovsky 2004) or O_4 (Acarreta et al. 2004) or by using the inelastic scattering signature (Joiner and Bhartia 1995). Measurements which have more than a certain amount of cloud are rejected and the others are corrected using the assumed vertical distribution of the absorber and modelled light path distribution.

The large area observed by current space-borne instruments in each individual measurement adds to the uncertainties in light path. Usually, a ground scene covered by one measurement is not homogeneous but varies in surface altitude, aerosol loading, surface albedo, absorber profile and concentration and, in particular, cloud cover. As a result, the *a priori* assumptions made cannot be correct for all parts of the scene and the retrieval results are a weighted average of the true absorber column density.

As the uncertainties in the light path are mainly the result of insufficient knowledge of the input parameters, they have both a systematic and a random component. Systematic errors are introduced for example by the use of the wrong vertical profile over an industrial area where emissions in the model are not up to date or if the albedo data base is incorrect. Random errors result from statistical variations in aerosol loading or cloud distributions. Consequently, averaging will reduce the effect of light path uncertainties but systematic errors will remain. It must also be realised that the use of *a priori* information from atmospheric models introduces a dependency of the retrieved data products on the model assumptions which is often undesirable.

2.5.5   *Uncertainty of Separation Between Stratosphere and Troposphere*

As discussed in Section 2.4, the separation of the tropospheric and stratospheric contributions to the atmospheric *VCD* utilizes external information or assumptions, which therefore introduce their associated uncertainty into the results. For example, how well the residual methods work depends on how homogeneous the stratospheric field is as a function of longitude. Overall in the stratosphere constituents are relatively homogeneously distributed in the tropics as a result of the stable

tropopause and strong winds, disturbed in mid-latitudes from tropospheric frontal systems, and strongly inhomogeneous in high latitudes in spring in the presence of the polar vortex. Systematic errors in the tropospheric VCDs are reduced by using model results or data assimilation to simulate the longitudinal dependence of the stratospheric column density but a residual source of uncertainty remains. Data smoothing and assimilation techniques run the risk of including large scale tropospheric pollution in the stratospheric field and so underestimate the tropospheric column densities for these situations. In general, it is difficult, if not impossible, to separate signals from the lower stratosphere and upper troposphere as one needs very good vertical resolution and accurate knowledge of the tropopause to do so. This is of significance for the retrieval of O_3 and BrO which have relatively large concentrations in the lower stratosphere.

Errors introduced from incomplete separation of stratospheric and tropospheric signals are systematic where they are linked to large scale dynamical structures but more random where they are linked to high and low pressure systems. The resulting errors are mainly additive and impact most strongly on retrievals for the remote unpolluted tropospheric conditions, and are less significant for regions with large tropospheric column densities.

2.6 Synopsis of the Historic, and Existing, Instruments and Data Products

In this section, a brief review of the most significant past and present generations of satellite instruments for tropospheric observations in the UV/vis/NIR is given. The objective of the first generation of satellite instruments for atmospheric sounding was the retrieval of stratospheric constituents and thus only a few representative missions are included here. Data from some of these instruments were, however, used in combination with information from other instruments to extract the tropospheric *VCD*s from total *VCD* observations. An overview of the satellite instruments is given in Appendix A; for a more detailed discussion see Burrows (1999).

During the last 30 years, the satellite-borne instrumentation has evolved with improvements of basic components: for example the collection/entrance optics, the dispersive element and the detector. Early instruments either had a static field of view (SBUV) or used a scanning mirror (TOMS) which moved orthogonally to the flight direction (the "whiskbroom" configuration). The light was dispersed by a prism and/or a diffractive grating and detected in distinct wavelength intervals by photo multiplier tubes or photodiode detectors (the slit position being moved to measure at different wavelengths). GOME, SCIAMACHY and GOME-2 all use a similar arrangement of the components on the optical bench with the dispersive element comprising a more complex configuration including a pre-dispersing prism building an intermediate spectrum within the instrument and splitting the wavelength range first into distinct parts. The spectral sub-windows are individually dispersed by

diffractive gratings coupled with focusing optics forming an image on one-dimensional photodiode arrays (Burrows et al. 1995; Burrows et al. 1999). For the SCIA-MACHY instrument, photodiode arrays for the near-IR spectral range between 1.0 and 2.4 μm were developed and used in space for the first time. A different instrumental design was used for the OMI instrument: instead of employing a scanning mirror to cover a swath perpendicular to the flight direction, a two-dimensional CCD detector is used (Levelt and Noordhoek 2002). One dimension of the detector covers the spectral information, while the other dimension covers the viewing direction perpendicular to the flight direction. This so called "pushbroom" configuration yields two-dimensional horizontal information without the necessity of having moving parts, but results in non-homogenous ground pixel sizes, which depend on the viewing angle.

2.7 Example of the Retrieval Process

In the following section, the retrieval process from UV/visible/NIR nadir measurements is illustrated with an example of tropospheric NO_2 derived from GOME-2 measurements made in March 2008. While details of the analysis vary for other trace gases, the overall approach is similar.

The tropospheric trace gas analysis for an individual satellite ground pixel starts with the measured intensities from the nadir observation and the direct sun measurement (Fig. 2.14a). First, the logarithm of the ratio is taken to determine the optical thickness (Fig. 2.14b) which is then converted into a differential optical thickness by subtraction of a suitable polynomial (Fig. 2.14b–c). In the next step, all known absorbers as well as a correction for the Ring effect are fitted to the optical depth to determine the slant column density of NO_2 (Fig. 2.14d–g). The remaining unexplained part of the signal, the residual, (Fig. 2.14h) is a measure of the quality of the fit. When this process is repeated for all measurements for a day or a month, a global map of NO_2 slant column densities is created (Fig. 2.15a). The slant column densities comprise the absorptions of stratospheric and tropospheric NO_2, and the effects of different light paths at different solar position and viewing geometry are not yet corrected. The slant column density over the Pacific region is assumed to represent the stratospheric column density and is subtracted at all longitudes from the total *SCD* (see box in Fig. 2.15a) yielding the tropospheric slant column density (Fig. 2.15b). As discussed in the previous sections, this is the simplest approach to stratospheric correction and more sophisticated methods can be used to reduce uncertainties. In this step, simultaneously a cloud filter of 0.2 (i.e. maximum cloud coverage of 20%) has been applied to remove those pixels which are strongly influenced by clouds. In the last step of the analysis, the height dependence of the measurement sensitivity needs to be accounted for by applying appropriate tropospheric *AMF*. As these depend on factors such as surface albedo, NO_2 profile and aerosol load, they are a function of time and location (see Fig. 2.15c). The final results of the analysis are the vertical tropospheric NO_2 column densities which are shown in Fig. 2.15d.
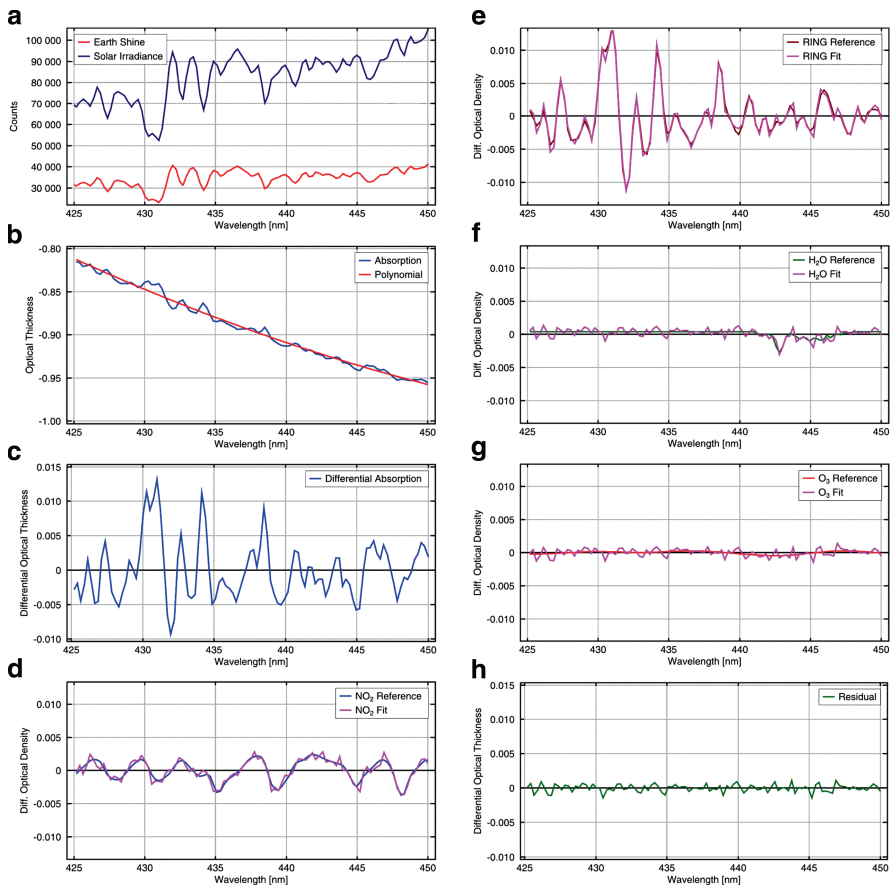
Fig. 2.14 Example of the spectral retrieval of NO_2 from a GOME-2 spectrum. See text for details.

In Fig. 2.15d, a number of interesting features can be discerned. High NO_2 column densities are observed over the industrialised parts of the world, in particular over China where rapid economic development has led to a strong recent increase in NO_x emissions. Enhanced tropospheric NO_2 is also observed over regions of intense biomass burning in Africa and parts of South America. The effect of lightning produced NO_x is not directly discernable but contributes to the high values in Africa. Another striking example of anthropogenic emissions is the thin line of NO_2 visible east of the tip of India, which is the result of ship emissions. There also are some regions with very low or even negative NO_2 column densities indicating that the assumptions made in the reference sector method for stratospheric correction are not adequate. For these regions more sophisticated analyses are necessary. A more detailed discussion of measurement results of tropospheric composition from space can be found in Chapter 8.
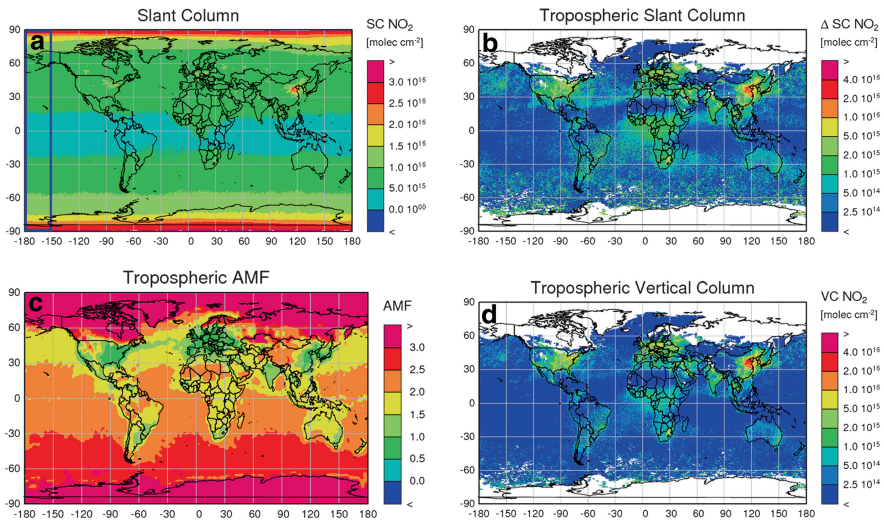
Fig. 2.15 Example of the NO_2 data analysis steps from the initial slant column density to the tropospheric vertical column density. The initial quantities are slant column densities (**a**) which are converted to tropospheric slant column densities (**b**) by subtracting the values over the reference sector (*blue box* in **a**). Application of the tropospheric AMF (**c**) yields the tropospheric vertical column densities (**d**). See text for details.

2.8 Future Developments

Although today's UV/vis/NIR satellite instruments already provide a wealth of useful data for atmospheric chemistry, numerical weather prediction and climate applications, it is interesting to consider, which components of the measurement and analysis system require further development to meet the growing needs of the scientific and operational communities. These are achieved by technical innovation with respect to optical design of the satellite instruments, innovative approaches for the retrieval algorithms and the data analysis and by the synergistic combination of data from complementary sensors.

2.8.1 Technical Design

In general it would be desirable to increase further the spatial and temporal resolution as well as the coverage of the measurements. For polar orbiting satellites, however, these properties are eventually limited by the available flux of reflected and backscattered solar photons. To achieve a sufficient signal to noise ratio, a compromise between global coverage and spatial resolution has to be made. Current UV/vis instruments like OMI and GOME-2 are close to the achievable limits: combining (almost) daily global coverage with spatial resolution (ground

pixel size) of the order of several hundred square kilometres. Some improvements can still be expected if larger detector areas and/or reduced spectral resolution are used, which would improve the signal to noise ratio. In contrast to the detectors used in the UV and visible spectral range, the quantum efficiency in the near IR might still be substantially improved, leading to improved signals facilitating higher spatial resolution (Fig. 2.16).
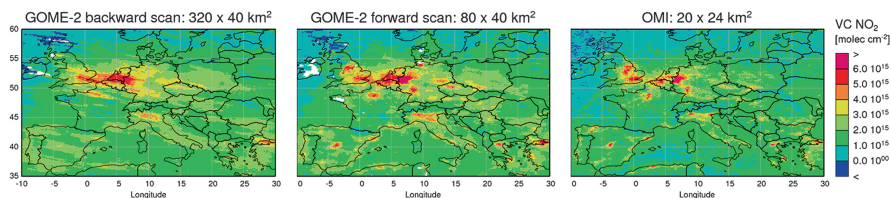

Fig. 2.16 Example of the effect of improved spatial resolution on the observed tropospheric NO_2 field over Europe. From *left* to *right*, spatial resolution is $320 \times 40\,km^2$ (GOME-2 data, only back-scan is used), $80 \times 40\,km^2$ (GOME-2 data, only forward scans are used), and $20 \times 40\,km^2$ (OMI data, only inner part of scan is used). With improving spatial resolution, more and more local hotspots can be identified while background values are slightly reduced. Note that OMI measurements are taken around noon while GOME-2 data are at 9:30 LT which introduces additional differences in the data, which do not result from spatial resolution.

In addition to polar orbiting satellites, it would be very desirable to operate geostationary satellites. These will allow much improved temporal resolution capturing, for example, the whole diurnal cycle (as long as daylight is available). Improvements in the spatial resolution using larger detectors and longer integration times than for low earth orbit instruments would be important for air quality applications, as well as improving the number of cloud free scenes. However, it should be realised that such satellites could only observe part of the globe and again a compromise between the spatial and temporal resolution and the spatial coverage has to be made.

Additional technical modifications might include the construction of instruments with well defined polarisation sensitivities. Such observations could yield improved information on the atmospheric radiative transfer and potentially add tropospheric profile information for O_3 (Hasekamp and Landgraf 2002). Also, the same ground scene could be observed under a variety of viewing angles. Such observations would allow an improved discrimination of aerosol scattering and surface reflection (Delderfield et al. 1986). In addition, for specific cases (with strong gradients and strong signals) tomographic inversion techniques could be applied. Such techniques have already been used for aerosol retrievals (Diner et al. 1998) but could be extended to trace gas observations. Finally, since the effect of aerosol scattering varies with viewing angle, additional profile information for trace gases might be extracted from the combined analysis of multiple-viewing observations.

Besides passive satellite instruments, active instruments might also be constructed. The extension of a lidar instrument (like CALIOP on CALIPSO) to

multi-wavelength observations (DIAL) might allow tropospheric trace gas observations with unprecedented vertical resolution albeit with reduced spatial coverage.

2.8.2   Data Analysis

Improvements of the data analysis might be achieved both for the spectral retrieval and the radiative transfer simulations. For the spectral retrieval, the available absorption cross-sections are still not of sufficient quality in many cases. Further laboratory measurements would lead to improved fitting results. Also the treatment of the effects of spectral surface reflectance and of Raman scattering (in the atmosphere and in the ocean) in the spectral fitting process still has limitations and should be improved.

For the radiative transfer simulations, improvements can be expected in the treatment of Raman scattering and polarisation. Improved input data should be sought, especially for the treatment of surface effects (albedo, topography, bidirectional reflection function) and information on aerosol and cloud properties. Also, the consideration of three dimensional gradients of trace gas concentrations, as well as better cloud and aerosol properties, will improve the interpretation of the satellite observations.

Finally, new methods could be used for the comparison between satellite observations and model results. Usually the retrieved trace gas results (or aerosol and cloud properties) are compared to corresponding data from atmospheric model simulations. Instead, the observational quantities (e.g. the spectral radiance or trace gas optical depths measured from satellite) could be calculated directly from the atmospheric model and then compared to the satellite observation. Such methods are especially interesting for data assimilation techniques.

2.8.3   Synergistic Use of Complementary Satellite Observations

From the combined use of information from different observations, many tropospheric data products could be improved substantially. Several combinations are possible: information from different wavelength ranges could yield improved information on the vertical profile. From the combination of observations at different overpass times, information on the diurnal cycle can be obtained as has been already demonstrated for OMI and SCIAMACHY (Boersma et al. 2008). Synergistic use of simultaneous measurements, for example with aerosols and NO_2 from the same platform, could improve the accuracy of the retrieved column densities. Another possible direction is the combination of instruments with high spatial resolution and low spectral resolution, with instruments optimised for trace gas observations. Such synergistic use would combine the benefits of both instruments.

References

Acarreta, J.R., De Haan, J.F., and Stammes, P., 2004, Cloud pressure retrieval using the O_2–O_2 absorption band at 477 nm, *J. Geophys. Res.*, doi:10.1029/2003JD003915.

Aliwell, S.R., M. Van Roozendael, P. V. Johnston, A. Richter, T. Wagner, D. W. Arlander, J. P. Burrows, D. J. Fish, R. L. Jones, K. K. Tornkvist, J.-C. Lambert, K. Pfeilsticker, and I. Pundt, 2002, Analysis for BrO in zenith-sky spectra; An intercomparison exercise for analysis improvement, *J. Geophys. Res.*, doi:10.1029/2001JD000329.

Beirle, S., Kühl, S., Puķīte, J., and Wagner, T., 2010, Retrieval of tropospheric column densities of NO2 from combined SCIAMACHY nadir/limb measurements, Atmos. Meas. Tech., **3**, 283–299, doi:10.5194/amt-3-283-2010.

Bhartia, P.K., R.D. McPeters, C.L. Mateer, L.E. Flynn, and C. Wellemeyer, 1996, Algorithm for the estimation of vertical ozone profiles from the backscattered ultraviolet technique, *J. Geophys. Res.,* **101**, 18793–18806.

Boersma, K. F., Eskes, H. J., Brinksma, E.J., 2004, Error analysis for tropospheric NO_2 retrieval from space, *J. Geophys. Res., Atmospheres*, doi:10.1029/2003JD003962.

Boersma, K. F., Eskes, H. J., Veefkind, J. P., Brinksma, E. J., van der A, R. J., Sneep, M., van den Oord, G. H. J., Levelt, P. F., Stammes, P. , Gleason, J. F., Bucsela, E. J., 2007, Near-real time retrieval of tropospheric NO_2 from OMI, *Atmos. Chem. Phys.*, **7**, 2103–2118.

Boersma, K.F., D.J. Jacob, H.J. Eskes, R.W. Pinder, J. Wang, and R.J. van der A, 2008, Intercomparison of SCIAMACHY and OMI tropospheric NO_2 columns: Observing the diurnal evolution of chemistry and emissions from space, *J. Geophys. Res.*, **113(D16)**, 14.

Bogumil, K., J. Orphal, T. Homann, S. Voigt, P.Spietz, O.C. Fleischmann, A. Vogel, M. Hartmann, H. Bovensmann, J. Frerik, and J.P. Burrows, 2003, Measurements of molecular absorption spectra with the SCIAMACHY pre-flight model: instrument characterization and reference data for atmospheric remote-sensing in the 230–2380 nm Region, *J. Photochem. Photobiol. A*, **157**, 167–184.

Bovensmann, H., J.P. Burrows, M. Buchwitz, J. Frerick, S. Noël, V.V. Rozanov, K. V. Chance, and A.H.P. Goede, 1999, SCIAMACHY - Mission objectives and measurement modes, *J. Atmos. Sci.,* **56(2)**, 127–150.

Bracher, A., M. Vountas, T. Dinter, J. P. Burrows, R. Röttgers, and I. Peeken, 2008, Quantitative observation of cyanobacteria and diatoms from space using PhytoDOAS on SCIAMACHY data, *Biogeosciences Discuss.*, **5**, 4559–4590.

Brewer A.C., C.T. McElroy, and J.B. Kerr, 1973, Nitrogen dioxide concentrations in the atmosphere, *Nature*, **246**, 129–133.

Buchwitz, M., Rozaonv, V.V., Burrows, J. P., 2000, A near-infrared optimized DOAS method for the fast global retrieval of atmospheric CH_4, CO, CO_2, H_2O, and N_2O total column amounts from SCIAMACHY ENVISAT-1 nadir radiances, *J. Geophys. Res. - Atmospheres*, **105(D12)**, 15231–15245.

Burrows, J.P., K.V. Chance, P.J. Crutzen, H. van Dop, J.C. Geary, T.S. Johnson, G.W. Harris, I.S.A. Isaksen, G.K. Moortgat, C. Muller, D. Perner, U. Platt, J.-P. Pommereau and H. Rohde, 1988, SCIAMACHY – A European proposal for atmospheric remote sensing from the ESA polar platform, *Max-Planck-Institute for Chemistry, Mainz, Germany.*

Burrows, J.P., E. Hölzle, A.P.H. Goede, H. Visser, W. Fricke, 1995, SCIAMACHY- Scanning imaging absorption spectrometer for atmospheric chartography, *Acta Astronautica*, **35(7)**, 445.

Burrows, J.P., 1999, Current and future passive remote sensing techniques used to determine atmospheric constituents, in A. F. Bouwman (editor), *Approaches to scaling trace gas fluxes in ecosystems*, Elsevier Science B. V., Amsterdam.

Burrows, J.P., Weber, M., Buchwitz, M., Rozanov, V., Ladstätter-Weißenmayer, A., Richter, A., DeBeek, R., Hoogen, R., Bramstedt, K., Eichmann, K.-U., Eisinger, M., Perner, D., 1999, The global ozone monitoring experiment (GOME): mission concept and first scientific results, *J. Atmos. Sci.,* **56**, 151–175.

Bucsela, E. J., Celarier, E.A., Wenig, M.O., Gleason, J.F., Veefkind, J.P., Boersma K.F., Brinksma, E.J., 2006, Algorithm for NO$_2$ vertical column retrieval from the ozone monitoring instrument, *IEEE Transactions on Geoscience and Remote Sensing*, **44(5)**, 1245–1258.

Cox, C., Munk, W., 1954, Measurements of the roughness of the sea surface from photographs of the sun's glitter, *J. Opt. Soc. Am.*, **44**, 838–850.

Cox, C., Munk, W., 1956, Slopes of the sea surface deduced from photographs of sun glitter, *Bull. Scripps Inst. Oceanography,* **6(9)**, 401–488.

Chance, K. V., Burrows, J.P., Perner, D., Schneider, W., 1997, Satellite measurements of atmospheric ozone profiles, including tropospheric ozone, from ultraviolet/visible measurements in the nadir geometry: A potential method to retrieve tropospheric ozone, *Journal of Quantitative Spectroscopy & Radiative Transfer*, **57(4)**, 467–476.

Chance, K., Kurosu, T.P., Sioris, C.E., 2005, Undersampling correction for array detector-based satellite spectrometers, *Applied Optics*, **44(7)**, 1296–1304.

Delderfield, J., Llewellyn-Jones, D. T., Bernard, R., de Javel, Y., Williamson, E. J., Mason, I., Pick, D. R. and Barton, I. J., 1986, The along track scanning radiometer (ATSR) for ERS-1, *Proc. SPIE*, **589**, 114–120.

DeBeek, R., M. Vountas, V.V. Rozanov, A. Richter, and J.P. Burrows, 2001, The Ring effect in the cloudy atmosphere, *Geophys. Res. Lett.*, **28**, 721–772.

Diner, D.J., J.C. Beckert, T.H. Reilly, C.J. Bruegge, J.E. Conel, R. Kahn, J.V. Martonchik, T.P. Ackerman, R. Davies, S.A.W. Gerstl, H.R. Gordon, J-P. Muller, R. Myneni, R.J. Sellers, B. Pinty, and M.M. Verstraete, 1998, Multi-angle Imaging SpectroRadiometer (MISR) description and experiment overview, *IEEE Trans. Geosci. Rem. Sens.*, **36 (4)**, 1072–1087.

ESA Publication Division (SP-1182), 1995, GOME, Global ozone monitoring experiment, users manual, edited by F. Bednarz, European Space Research and Technology Centre (ESTEC), Frascati, Italy.

Eskes, H.J., and K.F. Boersma, 2003, Averaging kernels for DOAS total-column satellite retrievals, *Atmos. Chem. Phys.*, **3**, 1285–1291.

EUMETSAT, GOME-2 Products Guide, 2005, http://www.eumetsat.int/en/area4/eps/product_guides/GOME-2/GOME2-PG.pdf.

Farman, J.C., B.G. Gardiner, and J.D. Shanklin, 1985, Large losses of total ozone in Antarctica reveal seasonal ClOx/NOx interaction, *Nature*, **315**, 207–210.

Fish, D.J., and R.L. Jones, 1995, Rotational Raman-Scattering and the Ring Effect in Zenith-Sky Spectra, *Geophys. Res. Lett.*, **22(7)**, 811–814.

Fishman, J., and J.C. Larsen, 1987, Distribution of total ozone and stratospheric ozone in the tropics - implications for the distribution of tropospheric ozone, *J. Geophys. Res., Atmospheres*, **92(D6)**, 6627–6634.

Frankenberg, C., U. Platt, and T. Wagner, 2005, Iterative maximum *a posteriori* (IMAP)-DOAS for retrieval of strongly absorbing trace gases: model studies for CH$_4$ and CO$_2$ retrieval from near infrared spectra of SCIAMACHY onboard ENVISAT, *Atmos. Chem. Phys.*, **5**, 9–22.

Frederick, J.E, R. P. Cebula, and D. F. Heath, 1986, Instrument characterization for the detection of long-term changes in stratospheric ozone: an analysis of the SBUV/2 radiometer, *J. Atmos. Oceanic Technol.*, **3**, 472–480.

Grainger, J.F., and J. Ring, 1962, Anomalous Fraunhofer Line Profiles, *Nature,* **193(4817)**, 762.

Hasekamp, O.P., and J. Landgraf, 2002, Tropospheric ozone information from satellite-based polarization measurements, *J. Geophys. Res., Atmospheres*, doi:10.1029/2001/JD001346.

Heath, D. F., Mateer, C. L., and Kreuger, A.J., 1973, The Nimbus-4 BUV atmospheric Ozone experiment- Two Year's operation, *Pure Appl Geophys*, **106–108**, 1238–1253.

Heath, D.F., A.J. Krueger, H.R. Roeder, and B.D. Henderson, 1975, The solar backscatter ultraviolet and total ozone mapping spectrometer (SBUV/TOMS) for Nimbus G, *Opt. Eng.,* **14**, 323–331.

Heath, D.F., Krueger, A.J., Park, H., 1978, The solar backscatter ultraviolet (SBUV) and total ozone mapping spectrometer (TOMS) experiment, in *The Nimbus 7 User's Guide*, NASA Goddard Space Flight Centre, MD, 175–211.

Hendrick, F., M. Van Roozendael, A. Kylling, A. Petritoli, A. Rozanov, S. Sanghavi, R. Schofield, C. von Friedeburg, T. Wagner, F. Wittrock, D. Fonteyn, and M. De Mazière, 2006, Intercomparison exercise between different radiative transfer models used for the interpretation of groundbased zenith-sky and multi-axis DOAS observations, *Atmos. Chem. Phys.*, **6**, 93–108.

Henyey, L., and J. Greenstein, 1941, Diffuse radiation in the galaxy, *Astrophys J.*, **93**, 70–83.

Hilsenrath, E., R.P. Cebula, M.T. Deland, K. Laamann, S. Taylor, C. Wellemeyer, and P.K. Bhartia, 1995, Calibration of the NOAA-11 Solar Backscatter Ultraviolet (SBUV/2) Ozone Data Set from 1989 to 1993 using In-Flight Calibration Data and SSBUV, *J. Geophys. Res.,* **100**, 1351–1366.

Hoogen, R., V.V. Rozanov, J.P. Burrows, 1999, Ozone profiles from GOME satellite data: algorithm description and first validation, *J. Geophys. Res.*, **104**, 8263–8280.

Hudson, R. D., and A. M. Thompson, 1998, Tropical tropospheric ozone from total ozone mapping spectrometer by a modified residual method, *J. Geophys. Res., Atmospheres*, **103(D17)**, 22129–22145.

Jiang, Y. B., and Y. L. Yung, 1996, Concentrations of tropospheric ozone from 1979 to 1992 over tropical Pacific South America from TOMS data, *Science*, **272(5262)**, 714–716.

Joiner, J., and P. K. Bhartia, 1995, The determination of cloud pressures from rotational Raman-scattering in satellite backscatter ultraviolet measurements, *J. Geophys. Res. - Atmospheres*, **100(D11)**, 23019–23026.

Joiner, J., Bhartia, P.K., Cebula, R.P., Hilsenrath, E., McPeters, R.D., Park, H., 1995, Rotational Raman-Scattering (Ring Effect) in Satellite Backscatter ultraviolet measurements, *Applied Optics*, **34(21)**, 4513–4525.

Joiner, J., and A.P. Vasilkov, 2006, First results from the OMI rotational Raman scattering cloud pressure algorithm, *Geoscience and Remote Sensing, IEEE Transactions*, **44**, 5, 1272–1282.

Kattawar, G.W., Young, A.T., Humphreys, T.J., 1981, Inelastic-scattering in planetary-atmospheres. 1. The ring effect, without Aerosols, *Astrophys. J.*, **243(3)**, 1049–1057.

Kirchhoff, G.R., 1859, Über die Fraunhoferschen Linien, Berichte der Königlichen Preußischen Akademie der Wissenschaften, **59**, 662.

Koelemeijer, R.B.A., J.F. de Haan, and P. Stammes, 2003, A database of spectral surface reflectivity in the range 335–772 nm derived from 5.5 years of GOME observations, *J. Geophys. Res.*, doi:10.1029/2002JD002429.

Koelemeijer, R.B.A., Stammes P., Hovenier J.W. and F.J. de Haan, 2010, A fast method for retrieval of cloud parameters using oxygen A-band measurements from the Global Ozone Monitoring Instrument, *J. Geophys. Res.*, D, **106**, 3475–3490.

Komhyr, W. D., Grass, R. D., and Leonhard, R. K., 1989, Dobson spectrophotometer 83: A standard for total ozone measurements, 1962–1987, *J. Geophys. Res.*, **94**, 9847–9861.

Krijger, J.M., M. van Weele, I. Aben, R. Frey, 2007, The effects of sensor resolution on the number of cloud-free observations from space, *Atmos. Chem. Phys.*, **7**, 2881–2891.

Kuze, A., and K.V. Chance, 1994, Analysis of cloud top height and cloud coverage from satellites using the O_2 A and B bands, *J. Geophys. Res.*, **99(D7)**, 14481–14491.

Leue, C., M. Wenig, T. Wagner, U. Platt, and B. Jähne, 2001, Quantitative analysis of NO_x emissions from GOME satellite image sequences, *J. Geophys. Res.*, **106**, 5493–5505.

Levelt P.F., and R. Noordhoek, 2002, OMI Algorithm Theoretical Basis Document Volume I: OMI Instrument, Level 0-1b Processor, Calibration & Operations, *Tech. Rep. ATBD-OMI-01*, Version 1.1.

Liu, X., K. Chance, C.E. Sioris, R.J.D. Spurr, T.P. Kurosu, R.V. Martin, and M.J. Newchurch, 2005, Ozone profile and tropospheric ozone retrievals from the global ozone monitoring experiment: algorithm description and validation, *J. Geophys. Res.*, doi:10.1029/2005JD006240.

Martin, R. V., K. Chance, D. J. Jacob, T. P. Kurosu, R. J. D. Spurr, E. Bucsela, J. F. Gleason, P. I. Palmer, I. Bey, A. M. Fiore, Q. Li, R. M. Yantosca, and R. B. A. Koelemeijer, 2002, An improved retrieval of tropospheric nitrogen dioxide from GOME. *J. Geophys. Res.*, **107(D20)**, 4437, doi:10.1029/2001JD001027.

McPeters, R.D., S.M. Hollandsworth, L.E. Flynn, J.R. Hermans, and C.J. Seftor, 1996, Long-term ozone trends derived from the 16 year combined NIMBUS 7/Meteor 3 TOMS version 7 record, *Geophys. Res. Lett.,* **23**, 3699–3702.

Meador, W.E., and Weaver, W.R., 1980, Two-stream approximations to radiative transfer in planetary atmospheres: A unified description of existing methods and new improvements, *J. Atmos. Sci.* **37**, 630–643.

Mie G, 1908, Beiträge zur Optik trüber Medien, speziell kolloidaler Metallösungen. Annalen der Physik, *Vierte Folge*, Band **25**, No. 3, 377–445.

Mishchenko, M.I., A.A., Lacis, L.D. Travis, 1994, Errors introduced by the neglect of polarization in radiative transfer calculations for Rayleigh scattering atmospheres, J. Quant. Spectrosc. Radiat. Transf., **51**, 491–510.

Müller, M. D., Kaifel, A.K., Weber, M., Tellmann, S., Burrows, J.P., Loyola, D., 2003, Ozone profile retrieval from Global Ozone Monitoring Experiment (GOME) data using a neural network approach (Neural Network Ozone Retrieval System (NNORSY)), *J. Geophys. Res., Atmospheres*, doi:10.1029/2002JD002784.

Noël, S., Buchwitz, M., Burrows, J.P., 2004, First retrieval of global water vapour column amounts from SCIAMACHY measurements, *Atmos Chem Phys*, **4**, 111–125.

Noxon, J. F., 1975, Nitrogen dioxide in the stratosphere and troposphere measured by ground-based absorption spectroscopy, *Science,* **189**, 547.

Noxon, J.F., Whipple Jr., E.C., and R.S. Hyde, 1979, Stratospheric NO 2.1. Observational method and behaviour at mid-latitude, *J. Geophys. Res.*, **84**, 5047–5065.

Palmer, P.I., D.J. Jacob, K. Chance, R.V. Martin, R.J.D. Spurr, T. Kurosu, I. Bey, R. Yantosca, A. Fiore, and Q. Li, 2001, Air-mass factor formulation for differential optical absorption spectroscopy measurements from satellites and application to formaldehyde retrievals from GOME, *J. Geophys. Res.*, 106, 17, 147–17,160.

Park, H., D.F. Heath, and C.L. Mateer, 1986, Possible application of the Fraunhofer line filling in effect to cloud height measurements, *Meteorological Optics, OSA Technical Digest Series*, 70–81, Opt. Soc. Am., Washington, D. C.

Perliski, L.M., and S. Solomon, 1993, On the evaluation of air mass factors for atmospheric near-ultraviolet and visible absorption spectroscopy, *J. Geophys. Res.,* **98**, 10363–10374.

Perner, D., D.H. Ehalt, H.W. Pätz, U. Platt, E.P. Röth, and A. Volz, 1976, OH-radicals in the lower troposphere, *Geophys. Res. Lett.,* **3**, 466–468.

Perner, D. and U. Platt, 1979, Detection of nitrous acid in the atmosphere by differential optical absorption, *Geophys. Res. Lett.*, **7**, 1053–1056.

Platt, U., D. Perner, and W. Pätz, 1979, Simultaneous measurements of atmospheric CH_2O, O_3 and NO_2 by differential optical absorption, *J. Geophys. Res.,* **84**, 6329–6335.

Platt, U., 1994, Differential optical absorption spectroscopy (DOAS), in M. W. Sigrist (Ed.), *Air Monitoring by Spectroscopic Techniques. Chemical Analysis Series,* John Wiley, New York, 127.

Platt, U., Marquard, L., Wagner, T., Perner, D., 1997, Corrections for zenith scattered light DOAS, *Geophys, Res. Lett*., **24(14)**, 1759–1762.

Platt, U, and Stutz, J., 2008, Differential optical absorption spectroscopy: principles and applications, Springer, Heidelberg.

Richter, A., Eisinger, E., Ladstätter-Weißenmayer, A., Burrows, J.P., 1999, DOAS Zenith sky observations: 2. Seasonal variation of BrO over Bremen (53°N) 1994–1995, *J. Atmos. Chem.*, **32(1)**, 83–99.

Richter, A., and J. P. Burrows, 2000, A multi wavelength approach for the retrieval of tropospheric NO_2 from GOME measurements, in *ERS-ENVISAT symposium, ESA publication SP-461*, edited, Gothenburg.

Richter, A., and J. P. Burrows, 2002, Tropospheric NO_2 from GOME measurements, *Adv Space Res* **29(11)**, 1673–1683.

Richter, A., Burrows, J. P., Nüß, H., Granier, C, Niemeier, U., 2005, Increase in tropospheric nitrogen dioxide over China observed from space, *Nature*, **437(7055)**, 129–132.

Roscoe, H. K., Fish, D.J., Jones, R.L., 1996, Interpolation errors in UV-visible spectroscopy for stratospheric sensing: Implications for sensitivity, spectral resolution, and spectral range, *Applied Optics*, **35(3)**, 427–432.

Rozanov, V.V., Kurosu, T., Burrows, J.P., 1998, Retrieval of atmospheric constituents in the UV-visible: A new quasi-analytical approach for the calculation of weighting functions, *J Quant Spectrosc Radiat Transf*, **60(2)**, 277–299.

Rozanov, V.V., A.A. Kokhanovsky, 2004, Semianalytical cloud retrieval algorithm as applied to the cloud top altitude and the cloud geometrical thickness determination from top of atmosphere reflectance measurements in the oxygen absorption bands, *J. Geophys. Res.*, doi: 10.1029/2003JD004104.

Sanghavi, S., 2003, An efficient Mie theory implementation to investigate the influence of aerosols on radiative transfer, Diploma thesis, University of Heidelberg, Germany.

Sarkissian, A., Roscoe, H. K., Fish, D., Van Roozendael, M., Gil, M., Chen, H. B., Wang, P., Pommereau, J.-P., and Lenoble, J., 1995, Ozone and NO_2 air-mass factors for zenith-sky spectrometers: Intercomparison of calculations with different radiative transfer models, *Geophys. Res. Lett.*, **22(9)**, 1113–1116.

Schoeberl, M.R., Ziemke, J.R., Bojkov, B., Livesey, N., Duncan, B., Strahan, S., Froidevaux, L., Kulawik, S., Bhartia, P.K., Chandra, S., Levelt, P.F., Witte, J. C., Thompson, A.M., Cuevas, E., Redondas, A., Tarasick, D.W., Davies, J., Bodeker, G., Hansen, G., Johnson, B.J., Oltmans, S. J., Voemel, H., Allaart, M., Kelder, H., Newchurch, M., Godin-Beekmann, S., Ancellet, G., Claude, H., Andersen, S.B., Kyrö, E., Parrondos, M., Yela, M., Zablocki, G., Moore, D., Dier, H., von der Gathen, P., Viatte, P., Stübi, R., Calpini, B., Skrivankova, P., Dorokhov, V., De Backer, H., Schmidlin, F.J., Coetzee, G., Fujiwara, M., Thouret, V., Posny, F., Morris, G., Merrill, J., Leong, C.P., König-Langlo, G., Joseph, E., 2007, A trajectory-based estimate of the tropospheric ozone column using the residual method, *J. Geophys. Res. - Atmospheres*, **112 (D24)**, 21.

Sierk, B., Richter, A., Rozanov, A., V. Savigny, C. Schmoltner, A.M. Buchwitz, M., Bovensmann, H., and J. P. Burrows, 2006, Retrieval and monitoring of atmospheric trace gas concentrations in nadir and limb geometry using the space-borne SCIAMACHY instrument, *Environ Monit Assess*, **120(1–3)**, 65–77.

Sioris, C. E., Kurosu, T.P., Martin, R.V., Chance, K., 2004, Stratospheric and tropospheric NO_2 observed by SCIAMACHY: first results, *Trace Constituents in the Troposphere and Lower Stratosphere*, **34(4)**, 780–785.

Solomon, S., A. L. Schmeltekopf, and R. W. Sanders, 1987, On the interpretation of zenith sky absorption measurements, *J. Geophys. Res.,* **92**, 8311–8319.

Slusser, J. R., K. Hammond, A. Kylling, K. Stamnes, L. Perliski, A. Dahlback, D. E. Anderson, and R. DeMajistre, 1996, Comparison of air mass computations. *J. Geophys. Res.,* **101**, 9315–9321.

van Noije, T. P. C., Eskes, H.J., Dentener, F.J., Stevenson, D.S., Ellingsen, K., Schultz, M.G., Wild, O., Amann, M., Atherton, C.S., Bergmann, D.J., Bey, I., Boersma, K.F., Butler, T., Cofala, J., Drevet, J., Fiore, A.M., Gauss, M., Hauglustaine, D.A., Horowitz, L.W., Isaksen, I.S.A., Krol, M.C., Lamarque, J.-F., Lawrence, M.G., Martin, R.V., Montanaro, V., Müller, J.-F., Pitari, G., Prather, M.J., Pyle, J.A., Richter, A., Rodriguez, J.M., Savage, N.H., Strahan, S.E., Sudo, K., Szopa, S., van Roozendael, M., 2006, Multi-model ensemble simulations of tropospheric NO_2 compared with GOME retrievals for the year 2000, *Atmos Chem Phys*, **6**, 2943–2979.

van de Hulst, H.C., 1981, Light scattering by small particles., New York, Dover, ISBN 0486642283.

Van Roozendael, M., Loyola D., Spurr R., Balis D., Lambert J-C., Livschitz Y., Valks P., Ruppert T., Kenter P., Fayt C., Zehner C., 2006, Ten years of GOME/ERS-2 total ozone data – The new GOME data processor (GDP) version 4: 1. Algorithm description, *J. Geophys. Res.*, **111**, D14311, doi:10.1029/2005JD006375.

Vasilkov, A. P., Joiner, J., Gleason, J., Bhartia, P.K., 2002, Ocean Raman scattering in satellite backscatter UV measurements, *Geophys. Res. Lett.*, doi:10.1029/2002GL014955.

Vountas, M., V.V. Rozanov, and J.P. Burrows, 1998, Ring effect: Impact of rotational Raman scattering on radiative transfer in Earth's Atmosphere, *J. Quant. Spec. Rad. Trans.*, **60(6)**, 943–961.

Vountas, M., A. Richter, F. Wittrock, and J.P. Burrows, 2003, Inelastic scattering in ocean water and its impact on trace gas retrievals from satellite data, *Atmos. Chem. Phys.*, **3**, 1365–1375.

Vountas, M., T. Dinter, A. Bracher, J. P. Burrows, and B. Sierk, 2007, Spectral studies of ocean water with space-borne sensor SCIAMACHY using Differential Optical Absorption Spectroscopy (DOAS), *Ocean Sci.*, **3**, 429–440.

Wagner, T., S. Beirle, M. Grzegorski, and U. Platt, 2007a, Satellite monitoring of different vegetation types by differential optical absorption spectroscopy (DOAS) in the red spectral range, *Atmos. Chem. Phys.*, **7**, 69–79.

Wagner, T., J. P. Burrows, T. Deutschmann, B. Dix, C. von Friedeburg, U. Frieß, F. Hendrick, K.-P. Heue, H. Irie, H. Iwabuchi, Y. Kanaya, J. Keller, C. A. McLinden, H. Oetjen, E. Palazzi, A. Petritoli, U. Platt, O. Postylyakov, J. Pukite, A. Richter, M. van Roozendael, A. Rozanov, V. Rozanov, R. Sinreich, S. Sanghavi, F. Wittrock, 2007b, Comparison of Box-Air-Mass-Factors and radiances for multiple-axis differential optical absorption spectroscopy (MAX-DOAS) Geometries calculated from different UV/visible radiative transfer models, *Atmos. Chem. Phys.*, **7**, 1809–1833.

Wendisch, M., and P. Yang, 2010, A Concise Introduction to Atmospheric Radiative Transfer, Wiley & Sons., ISBN: 978-3-527-40836-8.

Yang, K., X. Liu, N.A. Krotkov, A.J. Krueger, and S. A. Carn, 2009, Estimating the altitude of volcanic sulfur dioxide plumes from space borne hyper-spectral UV measurements, *Geophys. Res. Lett.*, doi:10.1029/2009GL038025.

Ziemke, J.R., Chandra, S., Bhartia, P.K., 1998, Two new methods for deriving tropospheric column ozone from TOMS measurements: Assimilated UARS MLS/HALOE and convective-cloud differential techniques, *J. Geophys. Res. - Atmospheres*, **103(D17)**, 22115–22127.

Ziemke, J. R., Chandra, S., Bhartia, P.K.,, 2001, Cloud slicing: A new technique to derive upper tropospheric ozone from satellite measurements, *J. Geophys. Res. – Atmospheres*, **106(D9)**, 9853–9867.